

Clay Diagenesis and Porosity Analysis of Shales

Mr. Jirapat Charoensawan

A Project Submitted in Partial Fulfillment of the Requirements for the
Bachelor Degree of Science Program in Department of Geology
Faculty of Science Chulalongkorn University Academic Year 2015
Copyright of Chulalongkorn University

การก่อกำเนิดใหม่ของแร่ดินและการวิเคราะห์ความพรุนของหินดินดาน

นาย จิรภัทร เจริญสุวรรณค์

โครงการนี้เป็นส่วนหนึ่งของการศึกษาตามหลักสูตรวิทยาศาสตรบัณฑิต ภาควิชาธรณีวิทยา
คณะวิทยาศาสตร์ จุฬาลงกรณ์มหาวิทยาลัย ปีการศึกษา 2558
ลิขสิทธิ์ของจุฬาลงกรณ์มหาวิทยาลัย

Project Title Clay Diagenesis and Porosity Analysis of Shales

By Mr. Jirapat Charoensawan

Field of Study Geology

Project Advisor Dr. Waruntorn Kanitpanyacharoen

Accepted by the Department of Geology, Faculty of Science, Chulalongkorn University in Partial Fulfillment of the Requirements for the Bachelor's Degree

.....Project Advisor

(Dr. Waruntron Kanitpanyacharoen)

นาย จิรภัทร เจริญสุวรรณ: การก่อตัวใหม่ของแร่ดินและการวิเคราะห์ความพรุนของหินดินดาน
(CLAY DIAGENESIS AND POROSITY ANALYSIS OF SHALES)
ที่ปรึกษาโครงการ: อาจารย์ ดร. วรยุทธ คณิตปัญญาเจริญ 42 หน้า

สาเหตุของการเกิดความดันเกินกำหนดในหินดินดานยังคงเป็นที่ถกเถียงเนื่องจากมีหลายปัจจัยที่สามารถทำให้เกิดความดันที่สูงเกินกว่าปกติได้ ปัจจัยที่ทำให้เกิดความดันเกินกำหนดนอกเหนือจากการอัดแน่นแบบไม่สมดุลและการเกิดน้ำมันและก๊าซธรรมชาติแล้ว การเพิ่มขึ้นของปริมาณของไหลในรูพรุนจากกระบวนการก่อตัวใหม่ของแร่ดินเป็นปัจจัยที่มีความซับซ้อนมากที่สุด ปริมาณแร่ดินนั้นมีความแปรปรวนมากในหินดินดานซึ่งไม่เป็นเนื้อเดียวกัน นอกจากนี้ ขนาดที่เล็กมากของแร่ดินทำให้การวิเคราะห์เชิงปริมาณทำได้ยาก การศึกษานี้จึงมีจุดประสงค์เพื่อศึกษาความสัมพันธ์ระหว่างการมีอยู่ของภาวะความดันเกินกำหนดและระดับการก่อตัวใหม่ของแร่ดินร่วมกับความพรุนของหินซึ่งเป็นที่อยู่ของของไหล ในการศึกษาจะนำตัวอย่างหินดินดานมาทำการทดลองด้วยวิธีซิงโครตรอนเอกซ์เรย์ดิฟแฟรคชันเพื่อหองค์ประกอบทางแร่ในหิน โดยผลการทดลองดังกล่าวแสดงให้เห็นว่าตัวอย่างนี้มีปริมาณแร่ดินเป็นช่วงที่กว้าง (15-60% โดยปริมาตร) ร่องค์ประกอบหลักที่พบคือ ควอตซ์ ซิเดอไรต์ คาโอลิไนท์ อิลไลต์-ไมกา และ อิลไลต์-สเม็คไทต์ ในขณะที่แร่ คลอไรต์ ไพไรต์ อัลไบต์ แคลไซต์และโดโลไมต์ เป็นองค์ประกอบรอง นอกจากนี้ยังพบการเปลี่ยนแปลงขององค์ประกอบตามระดับความลึกอีกด้วย อีกการทดลองหนึ่งคือการทดลองซิงโครตรอนเอกซ์เรย์ไมโครโทโมกราฟี เพื่อวิเคราะห์โครงสร้างจุลภาคและความพรุนของหิน ข้อมูลจากการทดลองนี้แสดงให้เห็นว่าตัวอย่างหินดินดานส่วนใหญ่มีความพรุนที่น้อย (0.4-2%) โดยที่ส่วนใหญ่เป็นรูพรุนประเภทรอยแตกระดับจุลภาค (0.2-1.2%) ในขณะที่หินดินดานมีรอยแตกมีความพรุนที่สูงกว่าอย่างมีนัยสำคัญ (~7.4%) ส่วนตัวอย่างที่เป็นหินทรายมีความพรุนในช่วง 7 ถึง 13% และสามารถจำแนกได้ว่าเป็นรูพรุนชนิดช่องว่างระหว่างเม็ดตะกอน ผลจากการทดลองทั้งหมดทำให้ทราบว่า การก่อตัวใหม่ของแร่ดินนั้นส่งผลต่อความดันในรูพรุนของหินเพียงเล็กน้อย นอกจากนี้ยังพบว่าระบบรูพรุนในหินดินดานนั้นมีความไม่ต่อเนื่องซึ่งช่วยให้เกิดการเพิ่มขึ้นของความดันได้

Department	Geology	Student's Signature
Field of Study	Geology	Advisor's Signature.....
Academic Year	2015	

553 27066 23: MAJOR GEOLOGY

Keyword: clay diagenesis, porosity, overpressure, Gulf of Thailand

JIRAPAT CHAROENSAWAN; CLAY DIAGENESIS AND POROSITY
ANALYSIS OF SHALES. PROJECT ADVISOR: DR. WARUNTORN
KANITPANYACHAROEN, 42 pp.

The origin of overpressure in shale has long been a debate as multiple factors are able to induce high pressure anomalies. Apart from the other overpressure-contributing factors including disequilibrium compaction and hydrocarbon generation, a rapid-increase of pore fluid volume through clay minerals diagenetic process is the most complex factor. The proportion of clay minerals vary greatly among heterogeneous shale. In addition, the extremely tiny grain size of clay minerals make quantitative analysis challenging. This study thus aim to investigate a relationship between overpressure, degree of clay diagenesis and the porosity of shale. A suite of 8 samples were first used in synchrotron X-ray diffraction (SXRD) experiment for mineral compositions identification. SXRD data show a broad range of clay mineral content (15-60 vol.%). The main minerals include quartz, siderite, kaolinite, illite-mica and illite-smectite while chlorite, pyrite, albite, calcite and dolomite serve as minor components. Moreover, synchrotron X-ray microtomography (SXRT) experiments were performed for 3D microstructure and porosity analysis. According to the SXRT data, most shale samples have very low porosity (0.4-2%) and are dominated by microfracture (0.2-1.2%). The fractured shale sample has significantly higher porosity (~7.4%). Porosity in sandstone samples range from 7 to 13% and can be categorized as an intergranular pore. Results from these experiments show that the clay diagenesis has minor impact on the shale pore pressure. However, discrete shale pore networks can enable pore pressure build up

Department Geology
Field of Study Geology
Academic Year 2015

Student's Signature

Advisor's Signature.....

Acknowledgements

The authors would like to thank Petroleum Authority of Thailand: Exploration and Production (PTTEP) for providing samples used in this study. We acknowledge the access to the facilities of the Advanced Photon Source and the Advanced Light Source for the synchrotron X-ray diffraction and synchrotron X-ray microtomography experiments respectively. We also appreciated the access to *MAUD* software used for analyzing the diffraction data as well as the *Simpleware ScanIP* for the tomographic data analysis. Lastly, I would like to give my sincere gratitude to Professor Waruntorn Kanitpanyacharoen, this project advisor, for conducting these complicated experiments, introduced and guided me through the complexities of the software and giving insightful advices for this project.

Contents

	Page
Abstract in Thai	iv
Abstract in English	v
Acknowledgements	vi
Contents	vii
List of Tables	viii
List of Figures	ix
Chapter I: Introduction	1
Chapter II: Study area and Methodology	7
2.1 <i>The Gulf of Thailand</i>	8
2.2 <i>Synchrotron X-ray diffraction</i>	10
2.3 <i>Synchrotron X-ray microtomography</i>	12
Chapter III: Results	14
3.1 <i>Synchrotron X-ray diffraction</i>	15
3.2 <i>Synchrotron X-ray microtomography</i>	19
Chapter IV: Discussion	24
4.1 <i>Clay diagenesis</i>	25
4.2 <i>Porosity analysis</i>	29
4.3 <i>Preferred orientation</i>	30
Chapter V: Conclusions	31
5.1 <i>Conclusions</i>	32
5.2 <i>Future works</i>	32
References	33
Appendices	35

List of Tables

	Page
Table 3.1 Tectosilicate and non-silicate mineral compositions	17
Table 3.2 Phyllosilicate mineral compositions and pole densities	17
Table 3.3 Reconstructed pole figure of phyllosilicate minerals.	18
Table 3.4 Gray scale values used in SXRT images segmentation	22
Table 3.5 Pore types classification	22
Table 4.1 Comparison between initial smectite volumes, degree of diagenesis and pore pressure gradients of the Gulf of Thailand and the Gulf of Mexico	28

List of Figures

	Page
Figure 1.1 Porosity-depth and pressure profile of overpressure.	3
Figure 1.2 Schematic diagram of smectite diagenesis reaction.	3
Figure 2.1 Location and stratigraphic sequences of the Gulf of Thailand.	9
Figure 2.2 Pore pressure-depth profile from the Pattani Basin and the North Malay Basin.	9
Figure 2.3 An example of Debye ring and 2D plot.	10
Figure 2.4 Schematic diagram of the SXRT experiment.	12
Figure 3.1 Comparison between experimental data and calculated data of 2D plot and diffraction peak profile.	16
Figure 3.2 A schematic diagram of the pole projection.	17
Figure 3.3 An example of tomographic data and gray scale distribution histogram.	20
Figure 3.4 Comparison between sandstone and shale tomographic data.	21
Figure 3.5 The spectrum of pore types.	21
Figure 3.6 Types of pore used for classification.	23
Figure 4.1 Cross plots between initial smectite and depth.	26
Figure 4.2 Kaolinite content in samples vs. depth.	26
Figure 4.3 An example of shale segmented 3D porosity model.	28
Figure 4.4 Total clay content vs. maximum, pole density cross plots	29
Figure 4.5 Cross plots between weight-average pole density and total clay content	30
Figure 6.1 A Diffraction peak profile and 2D spectra plot of sample #1	35
Figure 6.2 A Diffraction peak profile and 2D spectra plot of sample #2	36
Figure 6.3 A Diffraction peak profile and 2D spectra plot of sample #3	37
Figure 6.4 A Diffraction peak profile and 2D spectra plot of sample #4	38
Figure 6.5 A Diffraction peak profile and 2D spectra plot of sample #5	39
Figure 6.6 A Diffraction peak profile and 2D spectra plot of sample #6	40
Figure 6.7 A Diffraction peak profile and 2D spectra plot of sample #7	41
Figure 6.8 A Diffraction peak profile and 2D spectra plot of sample #8	42

Chapter I: Introduction

Introduction

Overpressure in shale has been a great challenge in petroleum exploration. Especially in drilling operation, overpressure is a main cause of well kick and blow out which can cause severe damage. In addition, the presence of overpressure can alter the whole rock physical properties causing an anomalies during the seismic interpretation processes. Several factors such as disequilibrium compaction, fluid expansion and clay diagenesis greatly contribute to overpressure. However, fluid expelled from clay diagenesis is one of the most complicated factor due to the heterogeneity and variety of shale compositions. This study aims to investigate a relationship between the existence of overpressure and portion of clay minerals, specifically illite and smectite, in shale samples derived from drilled wells using synchrotron X-ray diffraction (SXRD). Moreover, synchrotron X-ray microtomography (SXRT) is used to analyze pore volumes, geometry and distribution in order to understand where and how the fluids are stored

Overpressure occurs when the pore pressure rock strata exceeds the hydrostatic pressure trend. Based on the previous studies, the mechanism of pore pressure anomalies can be divided into two categories. The first mechanism is disequilibrium compaction, which is believed to be a primary factor causing an overpressure in a sedimentary basin (Osborne and Swarbrick, 1997). As the deposition of sediments progresses, along with an increase in vertical stress due to the sediment loading, the underlying sediments are compacted and their pore fluids are expelled from the pore space. If the rate of sediment compaction is comparable to the rate of fluid expulsion, a normal hydrostatic pore pressure is established (Fig. 1.1). However, in some particular depositional environments such as delta, the sedimentary deposition rate is more rapid than the rate of fluid expulsion. The pore fluids are unable to be expelled and thus remain trapped. The trapped fluids prevent the rocks from further compaction and results in overpressured strata.

Overpressure due to disequilibrium compaction can be predicted by using Eaton method (Eaton, 1972) which relies on a relationship between effective vertical stress and porosity. The effective vertical stress is a difference between lithostatic stress and internal fluid stress. A study by Tingay *et al.*, 2009 uses pore pressure data obtained from the formation pressure test and porosity data derived from sonic and density logs in the pore pressure prediction model. High porosity anomalies indicate the presence of overpressure as the rocks have undergone an under-compaction due to low vertical effective stress which is caused by high pressure trapped fluid (Tingay *et al.*, 2009). Thus, overpressure due to disequilibrium compaction can be reliably predicted by using wireline logging data.

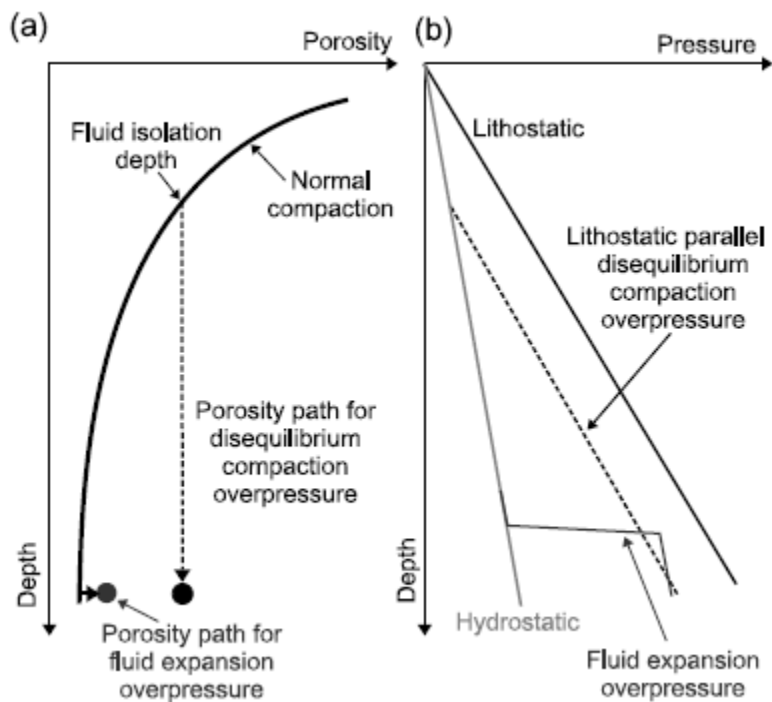


Figure 1.1 (a) Porosity-depth and (b) pressure profile of overpressure generated by disequilibrium compaction and fluid expansion (Modified from Tingay *et al.*, 2009)

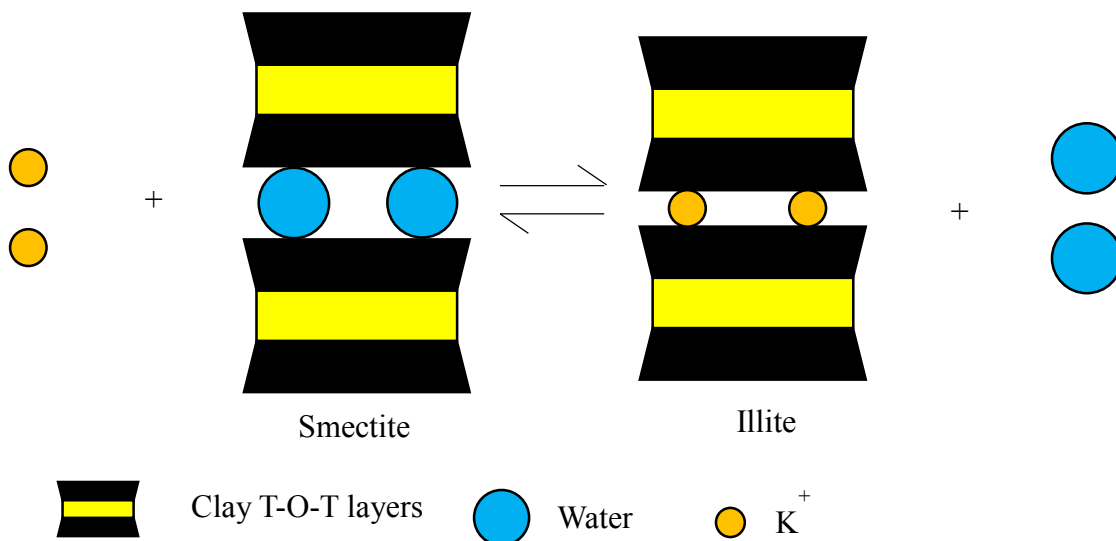


Figure 1.2 Schematic diagram of smectite diagenesis reaction (Hower *et al.*, 1976)

The second mechanism contributing to overpressure is fluid expansion. Fluid expansion refers to an increase in volume of pore fluids. In organic-rich shale, pore fluids are presented due to hydrocarbon generation and clay diagenetic processes. As the organic material or kerogen experiences high pressure and temperature conditions, it becomes more mature and releases hydrocarbon fluids and gases into pore or fracture spaces. The expelled hydrocarbon is unable to migrate and trapped in a limited space. Especially at the peak kerogen maturation, significant portion of kerogen is transform into fluid causing a significant increase in the rock pore pressure and porosity resulting in an overpressure (Osborne and Swarbrick, 1997).

Another mechanism that contribute to an increase in pore pressure is the smectite-to-illite transformation or clay diagenesis. Several previous studies use X-ray diffraction techniques to investigate the composition of clay-rich rocks and observe a wide variation in composition with depth (Hower *et al.*, 1976). For example, a decreases of smectite and K-feldspar volumes as well as an increase of illite and chlorite in mudrock from the Gulf of Mexico. The composition variation can be explained by the transformation of smectite $(\text{Na,Ca})_{0.33}(\text{Al,Mg})_2(\text{Si}_4\text{O}_{10})(\text{OH})_2 \cdot n\text{H}_2\text{O}$ into illite $(\text{K,H}_3\text{O})(\text{Al,Mg,Fe})_2\text{Si,Al}_4\text{O}_{10}(\text{OH})_2, (\text{H}_2\text{O})$. Both illite and smectite are phyllosilicate minerals with T-O-T structure comprise of an octahedral sheet in between two tetrahedral sheets. However, one of their differences is molecules between the T-O-T packages, K^+ ion for illite and water for smectite.

As smectite is exposed to high temperature during the subsidence, some aluminium atoms in octahedral sheets are substituted with silicon atoms, resulting in net positively charged layers (Fig. 1.2). To neutralize the charge balance between layers, the octahedral sheets thus need to get rid of water molecules between layers and replace them with small positive ions. Potassium atoms are generally present due to the weathering of K-feldspar and can be readily captured in the structure. A new mineral, Illite, is thus formed as a result of these chemical reactions (Hower *et al.*, 1976):



Another study of mudrock from the Gulf Coast, Texas, USA show that degree of smectite-to-illite transformation and the dissolution of k-feldspar increase with depth, as well as the amount of potassium content in the illite-smectite complex (Shaw and Primmer, 1989). The X-ray diffraction data show an increase in illite proportion in the illite-smectite complex. Moreover, the scanning electron microscopy (SEM) data show that the crystallization of authigenic kaolinite and chlorite are observed in both matrix and cavities, such as fossil porosity and corroded k-feldspar samples from the depth below clay diagenesis transition depth as well as the illite-smectite interlayering. However, the microprobe data indicate that amount of Fe^{2+}/Mg^{2+} in the illite-smectite increase with burial depth while the K^+ portion decreases. In contrast to the diagenetic reaction proposed by Hower *et al.* (1976), the reaction can be described by the following reaction (Shaw and Primmer, 1989):



Furthermore, a study by Bruce (1984) suggests that the top of overpressure zone in the Gulf Coast area is related to the top of smectite illitization reaction and the top of hydrocarbon generation. This study implies that the overpressure is caused by the dehydration of smectite layers along with oil and gas generation. Nonetheless, pressure build up from fluid expansion plays a great role in creating micro fracture which is essential for fluid migration. As the water is expelled from smectite layers during the diagenesis and move into restricted pore space, the fluid volume in the pore increase as well as the pore pressure. When the pressure reach a certain level, small cracks and fractures are generated in the rock matrix resulting in the pore fluid migration. While the causes of abnormal high pressure are in debate, one of the most important factor is an effective seal which prohibits the fluid transfer resulting in an accumulation of pore pressure. One of possible causes of fluid flow restriction is textural features (e.g. preferred orientation) which affect porosity and permeability of the rock as a whole (Ho *et al.*, 1999).

Unlike disequilibrium compaction, pore pressure prediction in a basin which significant pore pressure is generated by fluid expansion requires a thorough understanding of rock compositions. Such overpressure occurs in a local scale rather than basin-wide depending on the compositions such as proportion of kerogen or smectite and suitable environmental conditions (e.g. temperature) to trigger the fluid-expulsing mechanism. In practices, both factors influence high pressure formation. A study by Suwannasri *et al.* (2014) shows that velocity-vertical stress relationship can be used to estimate the fluid expansion-induced pressure. When the pore pressure caused by fluid expansion is taken into account and subtracted from measured pore pressure, the range of Eaton's exponent used in pore pressure prediction model reduces significantly and yield less uncertainty result. Thus, a better understanding in the mechanism of pore pressure generation by fluid expansion would help improve pressure prediction model.

The goal of this study is thus to investigate mineral compositions, texture and pore system of shale samples acquired from drilled well core and their relation to overpressure by using two experimental approaches. The first approach is using synchrotron X-ray diffraction experiment to quantify the mineral compositions and textures, especially clay minerals and their preferred orientation. The second experiment is synchrotron X-ray microtomography. The tomographic data is used to analyze porosity and pore types.

Chapter II: Study Area and Methodology

2.1 The Gulf of Thailand

Recently, the Gulf of Thailand has become the main source of off-shore Thai petroleum field due to the extensive petroleum exploration and production in the Basin area. The products includes mainly of gas and condensate. There are two main basins in the Gulf of Thailand area: the Pattani Basin and the North Malay Basin (Fig. 2.1a). The basins lie with the north-south to northwest-southeast trending due to the Late Eocene to Oligocene rifting events and consist of sedimentary packages which deposited after the rifting throughout the Cenozoic Era (Morley & Andrew, 2011). Both Basins consist of similar stratigraphic sequences. The oldest sedimentary sequence is *Sequence I*, which consists mostly of lacustrine shale with minor influx of fluvio-deltaic sedimentary rocks overlying above the pre-Tertiary basement. *Sequence II* overlies the first sequence with an abrupt transition. This sequence comprises of mudrock and sandstone deposited in various environment, including fluvial system, delta plain and intertidal which conformably overlain by *Sequence III*. The *Sequence III* was deposited during the sea level transgression, consist of fluvio-deltaic sediments with occasionally marginal marine deposits. The sedimentary rocks of *Sequence III* were later overlain by regression fluvio-deltaic sediments of *Sequence IV* which is predominated by sandstone and mudstone from fluvial and flood plain deposits due to the sea level regression. Lastly, the marginal marine deposits of *Sequence V* comprise of unconsolidated claystone mudstone and coal superimposed the *Sequence IV* unconformably according to the seismic data (Morley & Andrew, 2011) (Fig. 2.1b). Unfortunately, the petroleum exploration has encountered the problems regarding overpressure in both basins (Fig. 2.2) (Klahan and Nopsuri, 2012; Suwanasri *et al.*, 2014). In this study, shale samples are retrieved from drilled wells to analyze compositions microstructures, and 3D internal features using synchrotron X-ray diffraction and synchrotron X-ray microtomography techniques.

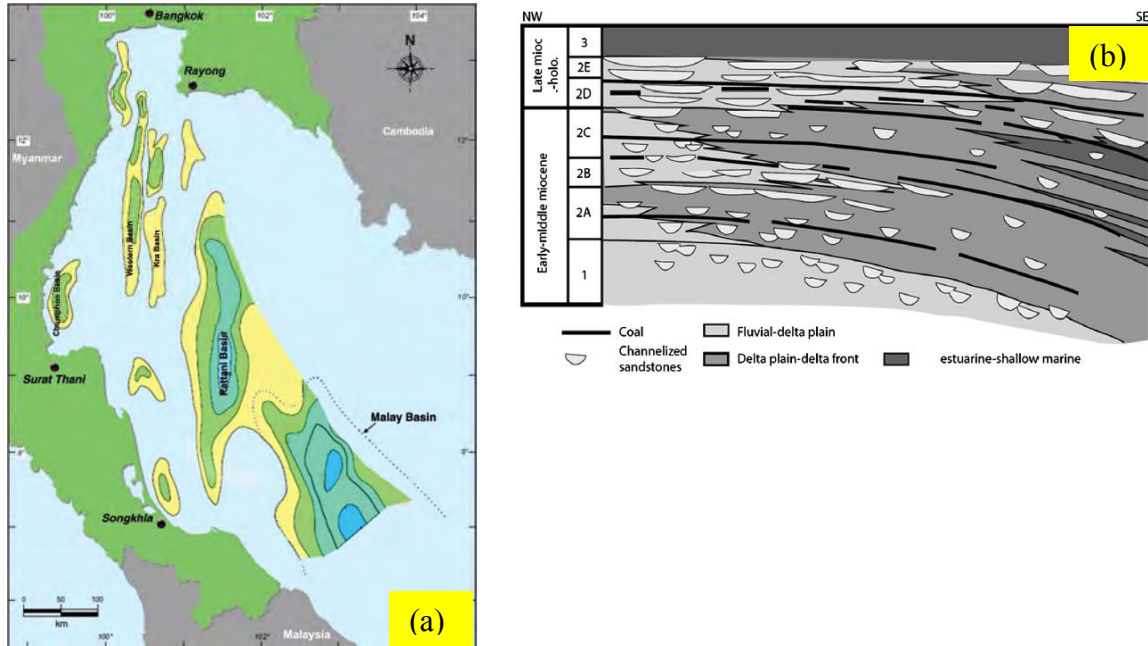


Figure 2.1 (a) Location of the sedimentary basin and (b) stratigraphic sequences of the Gulf of Thailand from *Sequence I* to *Sequence III*. (Modified from Tingay *et al.*, 2013; Suwanasri *et al.*, 2014).

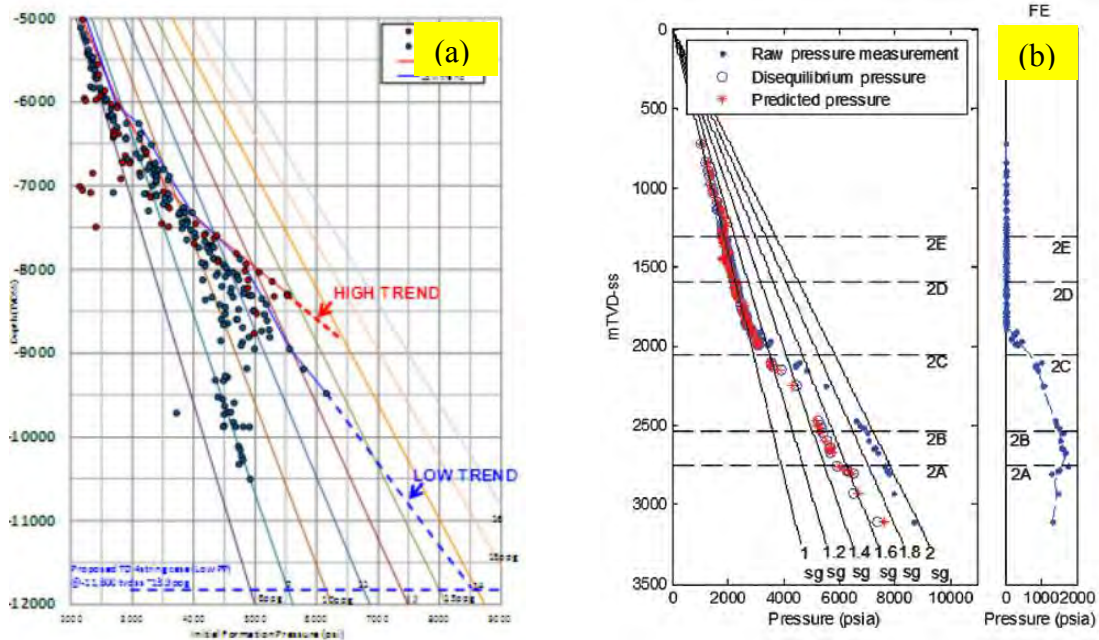


Figure 2.2 Pore pressure-depth profiles from (a) the Pattani Basin and (b) the North Malay Basin. (Modified from Klahan and Nopsuri, 2012; Suwanasri *et al.*, 2014)

2.2 Synchrotron X-ray diffraction

The first part is to investigate the mineral compositions using synchrotron X-ray diffraction (SXRD) technique. SXRD technique relies on Bragg's equation:

$$2d \sin \theta = n\lambda \quad \text{Equation 2.1}$$

Where d is lattice spacing, θ is scattering angle, n is a positive integer and λ is wavelength of X-ray beam. Each mineral contain a different set of lattice spacing (d) thus, result in a unique diffraction pattern. In particular, a variation of peak position (2θ) and peak height (intensity). The result of the SXRD experiments are recorded as Debye ring (Fig. 2.3a) which represent the diffraction patter of mineral compositions in the samples. As for clay minerals; the focus of this study, their (001) lattice planes are accounted for the low scattering angle peaks (low 2θ) due to their large lattice spacing (more than 7.40 Å) accordingly to the Bragg's law.

As a non-destructive method, SXRD method enable mineral preferred orientation analysis as well. Mineral preferred orientation is a selective alignment of mineral lattice planes in a certain direction which result in unevenly distributed intensity in the Debye ring (Fig. 2.3b). The preferred orientation can be displayed in pole figure.

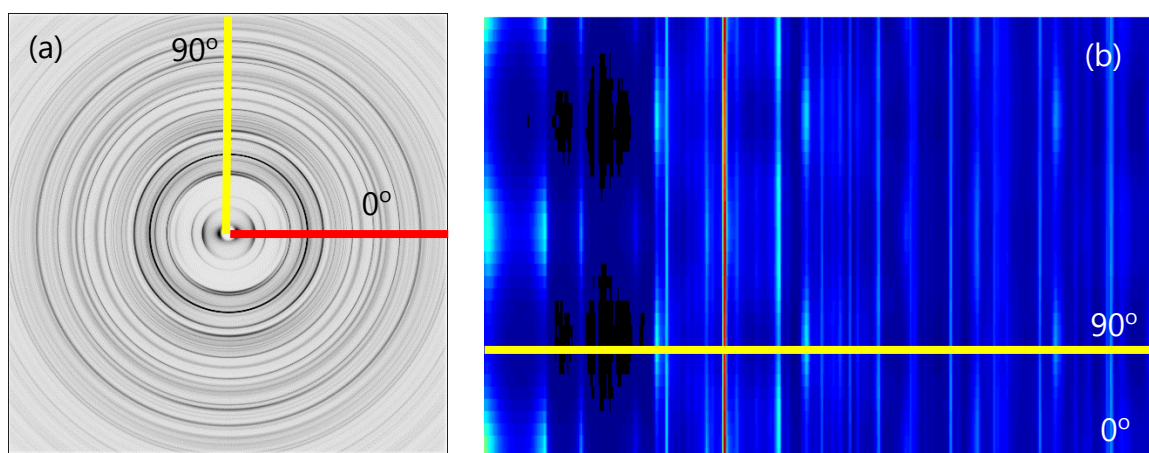


Figure 2.3 (a) An example of Debye ring recorded from the SXRD experiments and (b) an unrolled 2D plot of the Debye ring shows variation of X-ray intensity distribution which caused by respective preferred orientation of mineral phases.

For SXRD experiment, shale samples are cut into cylinders of 1 mm in diameter. The samples are mounted onto a rotatable platform aligned perpendicular to the X-ray incident beam. Next, monochromatic synchrotron X-ray of 0.111650 Å wavelength at the Advanced Photon Source (APS), Argonne National Laboratory (Chicago, Illinois, USA) are used to collect the diffraction data of the samples which are recorded for 60 seconds by the Mar345 detector placed about 2 meters away from the samples. Each Debye rings represent the diffraction pattern contain angle of 2θ ranged from 0 to 5 degree. The samples are then rotated around the cylindrical axis from -75° to 90° with 15° increment (-75° , -60° , -45° , -30° , -15° , 0° , 15° , 30° , 45° , 60° , 75° , 90° ; total of twelve data per sample) for pole figure reconstruction.

Debye rings collected from the experiment are integrated from the azimuth of 0° with 10° increment producing total of 36 spectra which represent the orientation of mineral lattice plane. The diffraction pattern are shown in Q-spacing ($Q = 2\pi/d$) instead of d-spacing in order to clearly distinguish the peak positions. Q-spacing ranged from 0.2 to 5 Å⁻¹ (1.26 to 31.42 d-spacing) are used in further calculation. The spectra are process with *MAUD* (Material Analysis Using Diffraction) software which relies Reitveld method, using least-square method to minimize the calculated model and the experimental data. Procedure used for quantitative data analysis can be summarized in these following steps.

- 1) Calibrate the instrumental parameters (sample-detector distance, beam tilt and image plate tilt) by using LaB₆ standard.
- 2) Import one out of twelve data (preferably an angle with high texture) and modify omega value accordingly to the angle of the data.
- 3) Import crystal structure datafiles of all composition phases base on peaks' position of the phases. The datafiles can be found in the American Mineralogist Crystal Structure database and *MAUD* database.
- 4) Refine background polynomial function and proportion of phases.
- 5) Refine phase microstructure including crystal size and microstrain based on isotropic modal and bound B-factor parameter.
- 6) Repeat steps 2) to 5) on the other data from the same sample.
- 7) Combine all twelve computational results of the same sample by importing all parameter files into one.
- 8) Calculate texture of phases with preferred orientation by using E-WINMV function with 10° orientation distribution function (ODF) resolution and without symmetry imposing.
- 9) Export the ODF files, remove calculation artifacts, smoothen and display pole figure using Beartex program.

2.3 Synchrotron X-ray microtomography

Second part is 3D porosity and internal micro-scale structures and features analysis by using synchrotron X-ray microtomography (SXRT). SXRT is a non-destructive method used for material fabric investigation which relies on Beer-Lambert law:

$$T = 10^{-A}; A = \epsilon cl \quad \text{Equation 2.2}$$

Where T is intensity of transmitted X-ray, A is absorbance, ϵ is molar absorptivity, c is amount concentration and l is path length of which the X-ray travel. Transmitted ray intensity is recorded as a gray scale images with gray scale value representing the absorbance of materials. The images can be further processed for phases and micro-structure analysis. In shale, low absorption features can be interpret as kerogen or void space (e.g. porosity and fracture), high absorption features usually represent heavy minerals such as pyrite while shale matrix including quartz and clay minerals are shown in wide-ranged medium value.

At the beginning of the SXRT experiment, several dark field images; images recorded without X-ray beam, and bright field images; images recorded with X-ray but without sample, are taken for detection of background noises and X-ray fluctuation for further correction. Next, shale samples cut in cylinders with 1 mm in diameter and 5 mm in length are mount onto the rotatable platform vertically in the middle of the field of view. Then X-ray beam is used to record the data. The transmitted X-ray is projected onto the scintillator which convert the X-ray into visible light and recorded as images projection (Fig. 2.4). The samples are then rotated by 180° with 0.120° increment for 3D images reconstruction coverage.

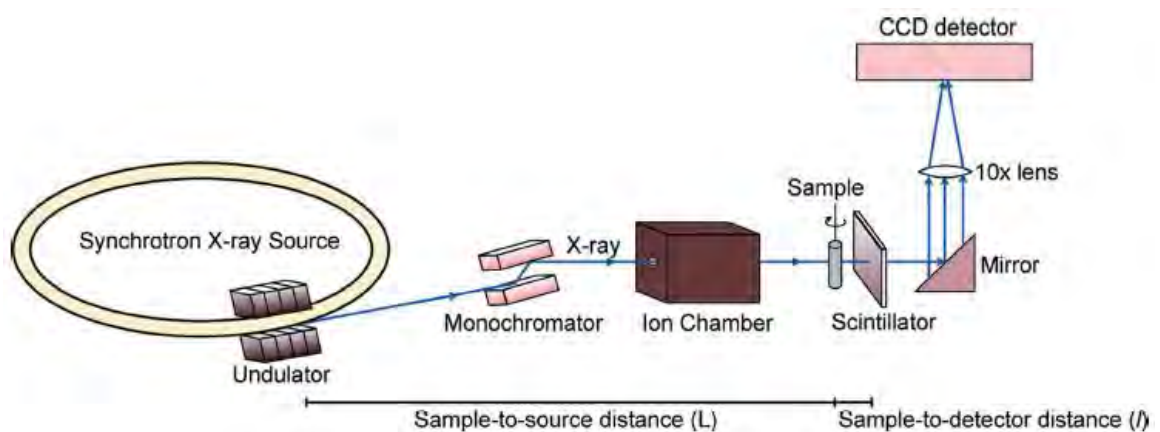


Figure 2.4 Schematic diagram of the SXRT experiment (Kanitpanyachoen *et al.*, 2012).

For 3D images reconstruction, raw projections are processed in the following step. The images are first processed with bright field and dark field images for background correction, removing X-ray fluctuation and instrumental artifacts by using the following equation:

$$I_c = [(I_r - I_d)(I_b - I_d)] \quad \text{Equation 2.3}$$

Where I_c is corrected image, I_r is raw image, I_d is dark field image and I_b is bright field image. Then, the images are normalized into the same gray scale value for all dataset by averaging values in the chosen area which contain no sample. Next, the normalized data containing all horizontal projection information were rearranged into sinogram. Lastly, the data were reconstructed into cross section images based on filtered back-projection algorithm into image files with a size of 2048 pixel x 2048 pixel and will be used for further images processing. In this study, *Simpleware SacnIP* is used for 3D tomographic data segmentation. Further image processing can be summarized in these following steps.

- 1) Import the images dataset to the program using a pixel size of 0.68 μm and 8-bit gray scale value.
- 2) Choose a region of interest of 0.34 x 0.34 x 0.34 mm^3 preferably from the center of the samples to avoid artificial features caused by sample preparation
- 3) Apply median filtering algorithm replacing a voxel gray scale value with the median of its own value along with neighboring voxels to minimize the calculation artifacts.
- 4) Classify features based on gray scale value and visual appearance using an image thresholding, flood fill and paint-with-threshold function to label every voxel with gray scale value within the threshold range as mask of interested features.
- 5) Perform an island removal function to eliminate any features which are smaller than 8 voxels which is considered as artifacts.

Chapter III: Results

3.1 Synchrotron X-ray Diffraction (SXRD)

The main purpose of SXRD analysis is to quantify the portion of mineral compositions as well as their preferred orientation by fitting the refined model with the experimental data (Fig. 3.1). Analysis of SXRD data show similarities in mineral compositions but wide range of volume proportion as summarized in Table 3.1 and Table 3.2. The mineral compositions can be divided into three groups: phyllosilicates or sheet-like silicate minerals (e.g. kaolinite illite and chlorite), tectosilicates (e.g. feldspars and quartz) and non-silicate minerals. Overall, the proportion of phyllosilicate mineral vary greatly (14 – 60 vol.%) and is dominated by illite-mica (8 – 35 vol.%). A significant kaolinite/dickite (7 - 13 vol. %) and illite-smectie (5 – 14 vol.%) is presented in majority of sample while chlorite (1 – 3 vol.%) is only presented in as a minor phase in a few samples. In addition to phyllosilicates, quartz is notably observed in all samples (28 – 77 vol.%). Siderite (FeCO_3) is another important mineral, found in large amount in sample #1 and #8 at 23 vol.% and 35 vol.%, respectively. However, other sample contain a small portion of siderite (1 – 8 vol.%). Some samples also contain a few percentages of pyrite (0.7 – 1 vol.%), calcite (~ 3 vol.%) dolomite (3 – 8 vol.%) and Albite (2 – 4 vol.%).

To better understand the behaviors and diagenesis of phyllosilicates, which are the dominant phases in samples, SXRD data are further analyzed for crystallographic preferred orientation. Preferred orientation results are present as pole figures. Reconstructed pole figures from SXRD analyses show that the (001) lattice planes of phyllosilicates minerals are preferentially aligned parallel to the bedding plane. The magnitudes of (001) preferred orientation are however variable in samples (Table 3.3). All monoclinic phases e.g. illite-mica and illite-smectite are displayed in the second-setting, where the c-axis acts as a unique axis thus, making (100) lattice plane show the maximum pole density. In contrast, tectosilicate and non-silicate minerals show no evidence of preferential orientation. It is thus concluded that quartz, feldspar, pyrite, calcite, and siderite are randomly oriented in the matrix.

Pole figure contains important information about the orientation distribution function of specific lattice places. This probability function describes the magnitude of finding “poles” or “lattice normals” preferentially oriented in a certain direction. Pole figure is normally represented as a projection of poles of a specific lattice plane onto an upper hemisphere and further projected onto a two dimensional plane (Fig. 3.2). The pole density is measured in multiple of random distribution (m.r.d.). The maximum pole densities of each phyllosilicate minerals are summarized in Table 3.3. In most samples, either illite-mica (1.3 – 5.4 m.r.d.) or chlorite (1.9 – 3.9 m.r.d.) show relatively high degree of preferred orientation with maximum pole density of 5.4 and 3.9 m.r.d. respectively. For kaolinite and dickite, they show similar intermediate preferred orientation (1.1 – 4.5 m.r.d.) while illite-smectite (1.4 – 3.9 m.r.d.) displays the least magnitude of preferred orientation in most samples.

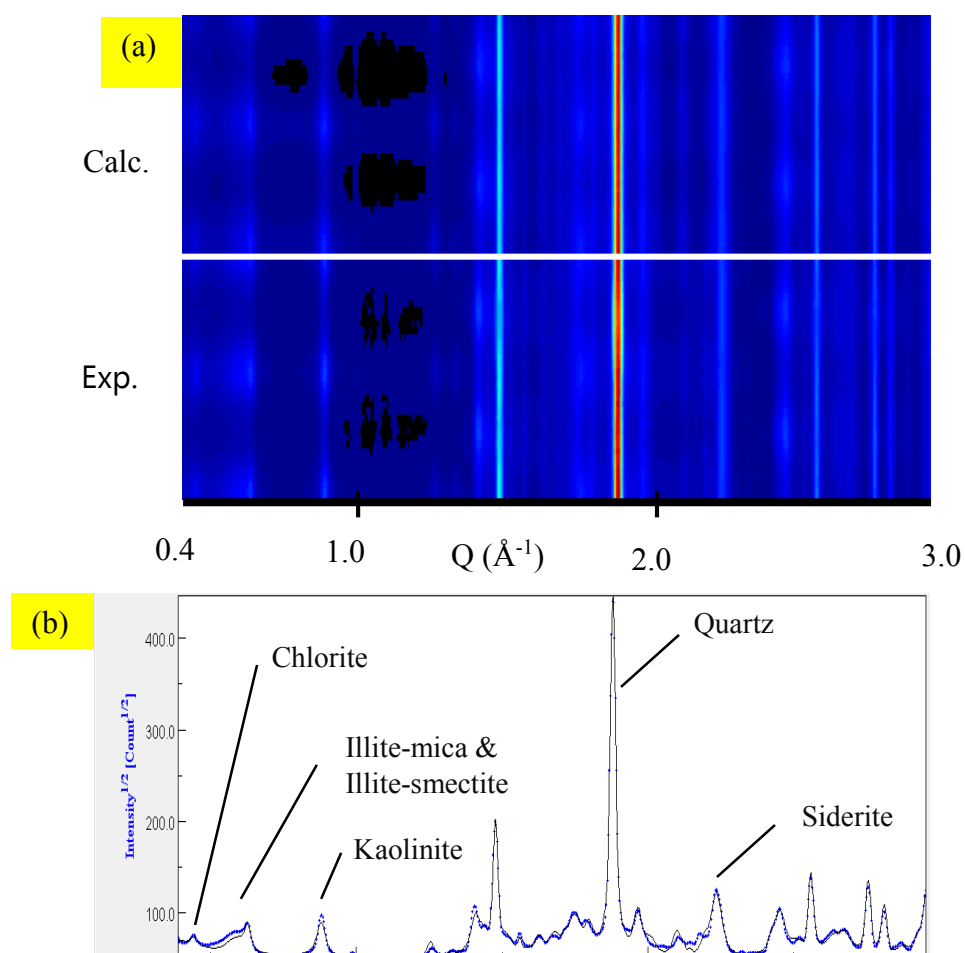


Figure 3.1 (a) Comparison of unrolled 2D spectra of sample #3 between calculated data (upper) and experimental data (lower) and (b) peak profile of the same data showing calculated data (black line) and experimental data (blue line).

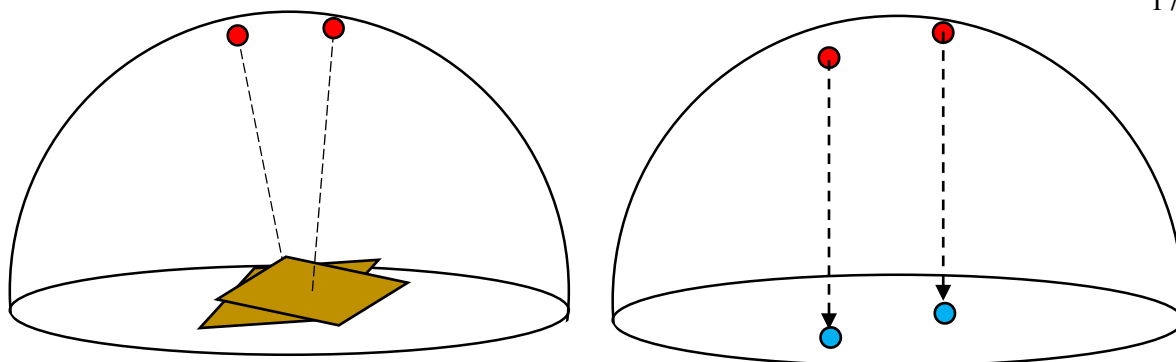


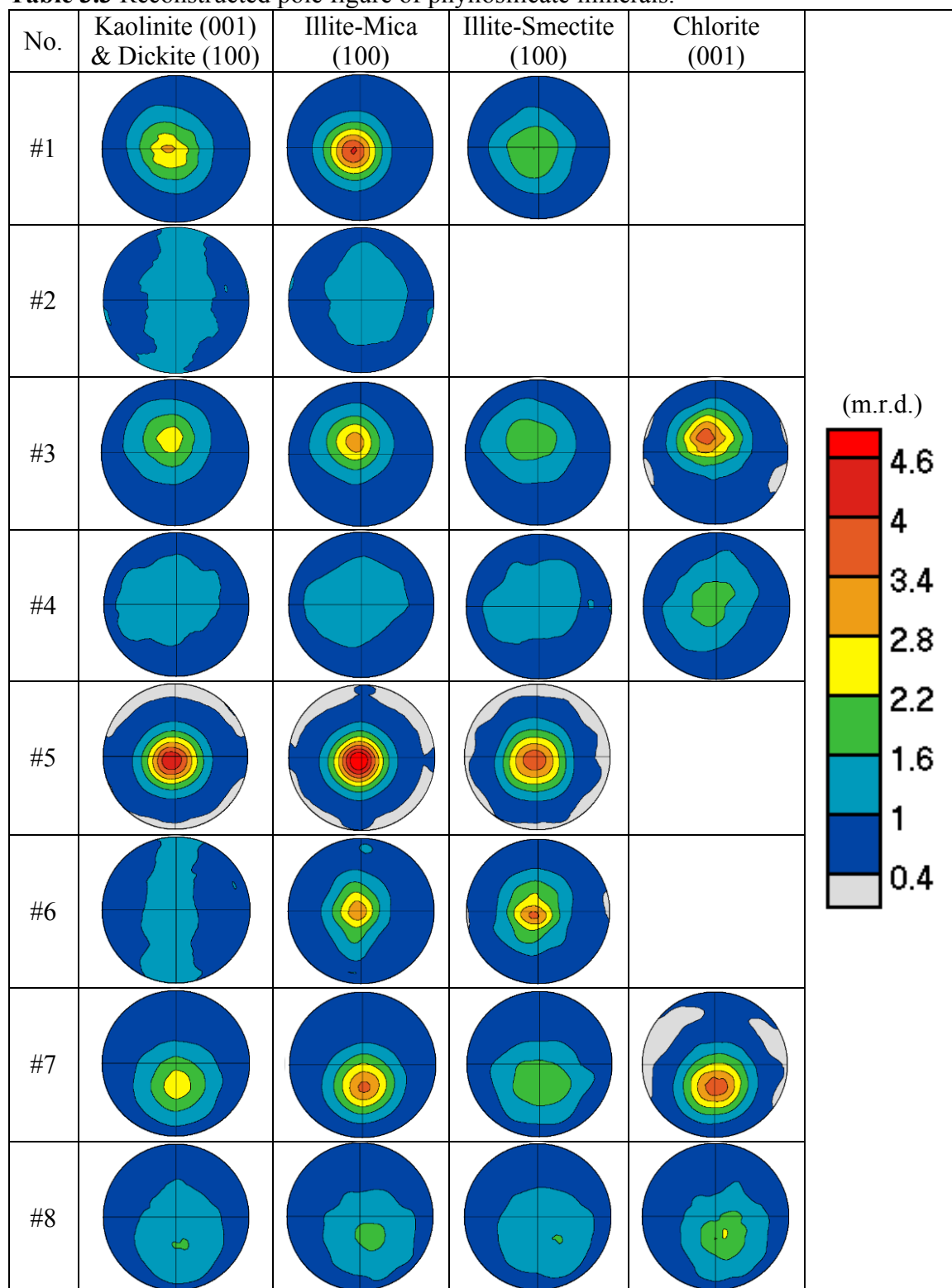
Figure 3.2 A schematic diagram of the pole projection. The normal lines are projected from the planes (brown) onto the sphere (red) which are further projected onto the two dimension plane (blue).

Table 3.1 Tectosilicate and non-silicate mineral compositions (vol. %).

No.	Quartz	Siderite	Pyrite	Albite	Calcite	Dolomite	Total
#1	31.27	23.09					54.36
#2	76.27	0.89				8.24	85.40
#3	49.26	5.66		3.09			58.01
#4	58.65			3.81			62.46
#5	29.70	8.32	0.70	1.63			40.35
#6	60.46	8.43	0.72	2.36		2.78	74.75
#7	34.64	3.80		2.37	3.08	3.90	47.79
#8	27.58	34.60	1.01				63.19

Table 3.2 Phyllosilicate mineral compositions (vol.%), maximum pole density for each phases are shown in parentheses (m.r.d.).

No.	Kaolinite & Dickite	Illite-Mica	Illite-Smectite	Chlorite	Total	Error (%)
#1	8.05 (2.88)	28.29 (3.93)	9.30 (2.03)		45.64	12.42
#2	6.94 (1.05)	7.65 (1.30)			14.59	13.81
#3	9.99 (2.49)	19.91 (3.12)	10.29 (2.02)	1.80 (3.93)	41.99	11.23
#4	6.87 (1.25)	17.40 (1.48)	10.33 (1.39)	2.93 (1.90)	37.53	11.93
#5	9.72 (4.49)	35.58 (5.43)	14.35 (3.91)		59.65	13.71
#6	10.18 (1.24)	10.27 (3.44)	4.79 (3.63)		25.24	16.62
#7	11.15 (2.55)	24.87 (3.26)	13.09 (2.00)	3.09 (3.04)	52.20	11.60
#8	12.86 (1.61)	12.92 (1.79)	10.52 (1.60)	0.50 (2.34)	36.80	11.46

Table 3.3 Reconstructed pole figure of phyllosilicate minerals.

3.2 Synchrotron X-ray microtomography (SXRT)

SXRT data are used to reconstruct 3D internal features of the samples and analyzed volume fractions, morphology, and distribution of constituent phases that cannot be quantified by the SXR method. Image segmentation is applied to distinguish different phases in the samples. This approach classifies different features based on their grayscale values. Low x-ray absorbing materials normally have low grayscale values and are classified as pore, fracture, or kerogen. High grayscale values thus indicates high x-ray absorbing features such as heavy minerals (Fig. 3.3a). However, a distinct separation of phases that have low and moderate grayscale values e.g. clay minerals and the matrix (Fig. 3.3b), is very challenging to obtain. The histogram of grayscale values has many overlapping peaks. It is thus necessary to use visual classification in addition to computational segmentation approach. A summary of 3D segmentation results is shown in Table 3.4. The samples can be classified into two rock types based on microstructure and phase volumes. The first group represents sandstone with large grain size approximately 0.1 mm (Fig. 3.4a). The pore space in this rock type is generally large and can be clearly observed by eyes. The second group shows fine to very fine grain sizes, which are quite indistinguishable from the matrix (Fig. 3.4b). This group is classified as shale and mudstone. Sandstone also contains almost no kerogen but high total porosity (pore + kerogen), ranging from ~7 to ~13%, while shales have considerably lower total porosity (~1~2%) and mostly comprise of small discrete kerogen-filled pores and dispersed randomly in the matrix. Sample #3 however, contains a large amount of connected fractures and fracture-parallel kerogen. The presence of kerogen and fracture contribute to high total porosity (~7%) in this sample.

Pores are categorized further into different pore types based on their distribution and morphology. A study by Loucks *et al.*, 2012 shows different pore types from nano to microscales which are used as guidelines for pore classification in this study (Fig. 3.5). However, some pore types are unable to be classified due to the resolution limit of the data (e.g. kerogen pores and corroded-grain pores) or the lack of host features (e.g. pellet pores and moldic pores). The main, pore types in our samples include inter granular pore, fracture pore, fossil pore, framboidal pore, irregular pore and micro-pore as summarized in Table 3.5 (Fig. 3.6). For sandstones, only intergranular pores can be classified as they are composed mainly of quartz grains. On the other hand, shales samples are dominated by fracture pore, micro-pore and irregular pore are also common as well. The other pore types are feature-dependent, meaning their portions are based on the compositions of the rock.

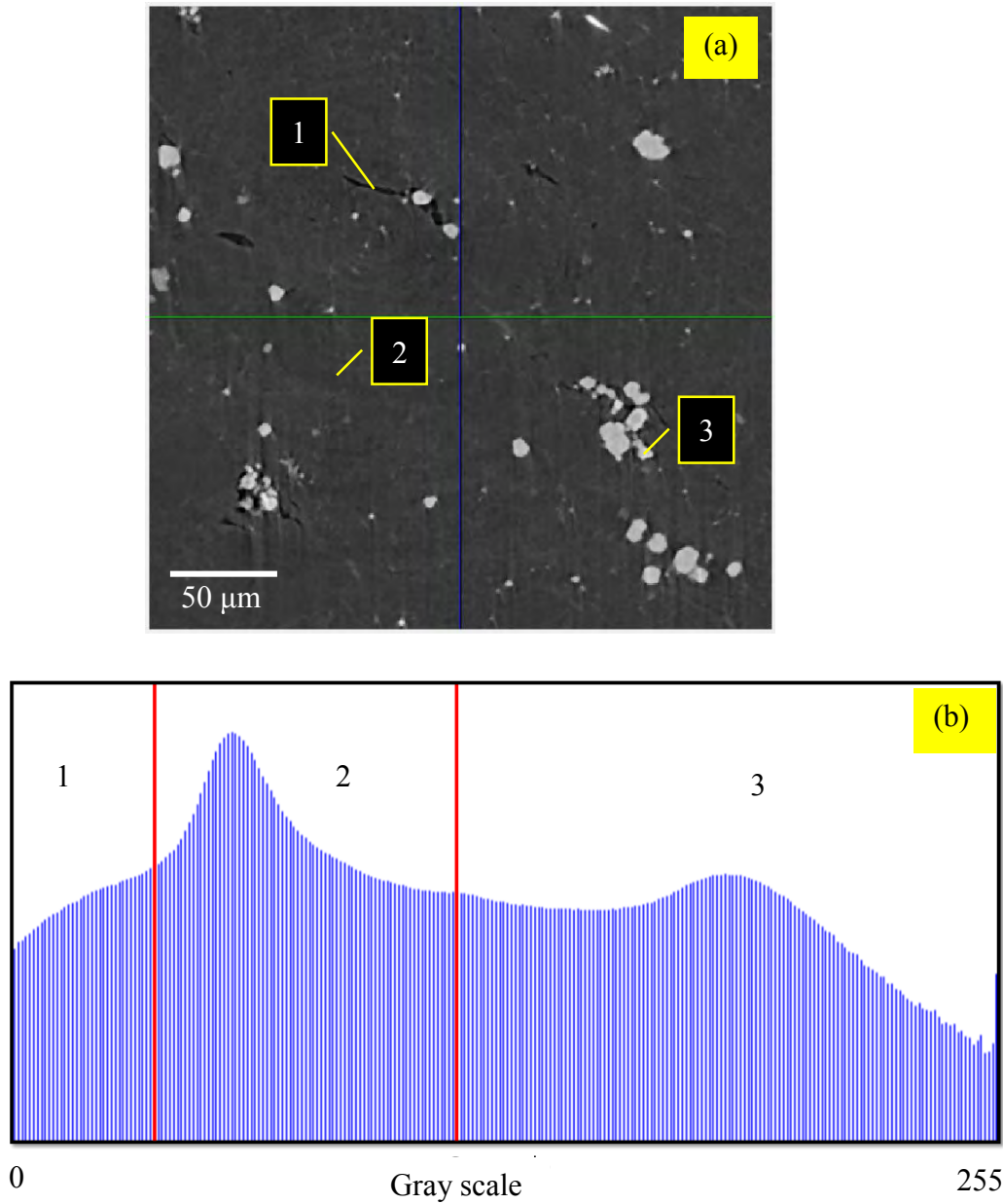


Figure 3.3 (a) An example of tomographic data and (b) histogram showing grayscale value distribution of the data. The numbers indicate the range of value used for segmentation different phases, whereas [1] pore, [2] matrix and [3] pyrite. The size of the tomographic image is 0.34 x 0.34 mm².

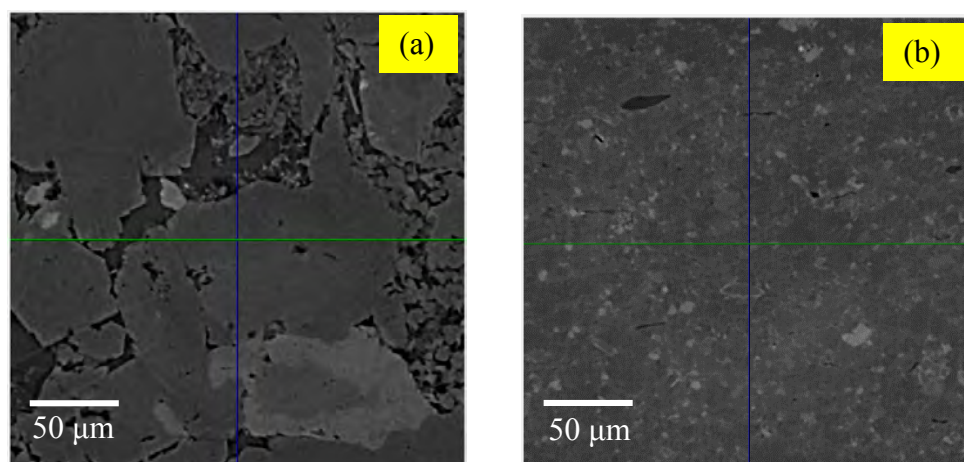


Figure 3.4 Comparison between tomographic images of (a) sandstone with larger grain size and (b) shale. The size of the tomographic image is $0.34 \times 0.34 \text{ mm}^2$.

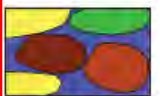
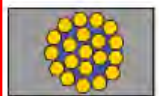









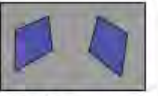
A		Organic-Matter Pores	Fracture Pores
Mineral Matrix Pores Pores between or within mineral particles		Pores within organic matter	Pores not controlled by individual particles
Interparticle Pores	Intraparticle Pores	Organic-Matter Pores	Fracture Pores
 <p>Pores between grains</p>	 <p>Intercrystalline pores within pyrite framboids</p>		
 <p>Pores between crystals</p>	 <p>Pores within peloids or pellets</p>		
 <p>Pores between clay platelets</p>	 <p>Pores within fossil bodies</p>		
 <p>Pores at the edge of rigid grains</p>	 <p>Moldic pores after a fossil</p>		
	 <p>Intraplatelet pores within clay aggregates</p>		
	 <p>Dissolution-rim pores</p>		
	 <p>Moldic pores after a crystal</p>		

Figure 3.5 The spectrum of pore types. The pore types presented in this study are marked in red (modified from Loucks *et al.* 2012).

Table 3.4 Minimum and maximum gray scale value used for the segmentation for all sample are close-ranged. The segmented mask can be used to calculate further for volume percentages.

Sample	Pore			Kerogen			Total (Vol.%)
	Min	Mix	Vol.%	Min	Mix	Vol.%	
#1	0	28	0.05	29	46	0.37	0.42
#2	0	42	13.27	-	-	-	13.27
#3	0	20	1.04	21	46	6.62	7.66
#4	0	46	7.31	-	-	-	7.31
#5	0	30	0.34	31	46	1.42	1.76
#6	0	30	0.13	31	41	0.79	0.92
#7	0	30	0.24	31	45	0.84	1.06
#8	0	32	0.41	33	42	0.48	0.89

Table 3.5 Pore types classification for each samples displayed in vol.%. Sandstones are marked with an asterisk.

Sample	Fracture	Irregular	Fossil	Framboid	Intergranular	Micro	Total
#1	0.20	0.16	0.02	-	-	0.04	0.42
#2*	-	-	-	-	13.27	-	13.27
#3	5.26	0.37	-	-	-	2.04	7.66
#4*	-	-	-	-	7.315	-	7.31
#5	1.18	0.13	-	-	-	0.51	1.76
#6	0.46	0.36	0.13	-	-	0.30	0.92
#7	0.65	0.05	-	-	-	0.33	1.06
#8	0.34	0.19	-	0.30	-	0.07	0.89

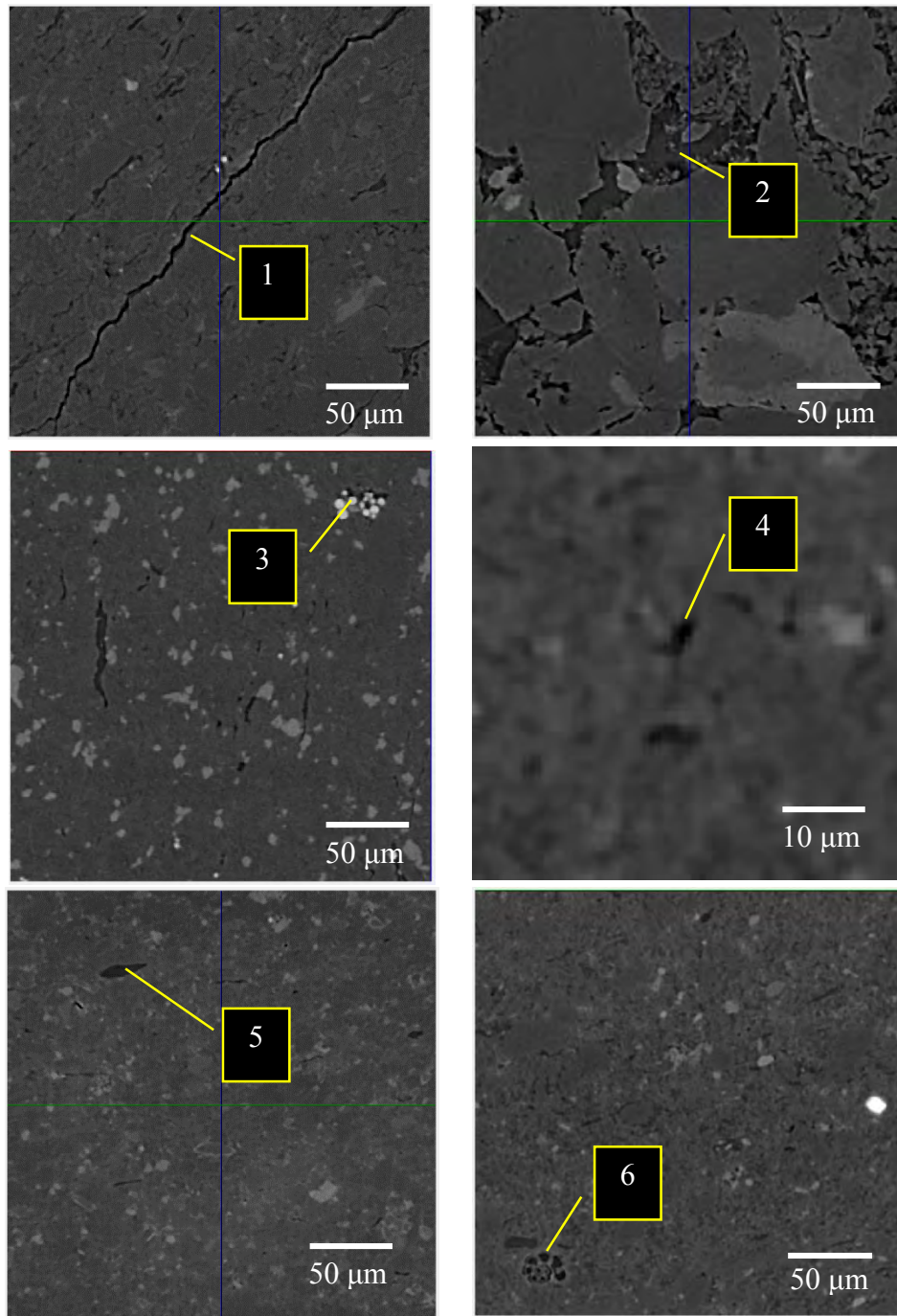


Figure 3.6 Types of pore used for classification including [1] fracture pore, [2] intergranular pore, [3] framboidal pore, [4] micro-pore and [5] irregular pore and [6] fossil pore.

Chapter IV: Discussion

4.1 Clay diagenesis

The main focus of this study is to determine the influences of expelled water from clay diagenesis reaction to the increase of pore pressure in shale. According to smectite-to-illite transformation reaction, the amount of water released from the process is related to the amount of smectite that is transformed into illite. Two factors that largely govern the process are the degree of smectite diagenesis and the proportion of initial smectite in the pre-diagenetic phase. Even though the initial portion of smectite is unable to measure directly, based on an assumption that the initial compositions of shale and mudrock include pure phase smectite, pure phase detrital illite-mica and other components. As the diagenesis progresses, smectite is gradually transformed into illite-smectite complex and ultimately become pure illite or further react with muscovite to become illite-mica. Thus, the initial smectite proportion is estimated from the summation of illite-smectite and illite-mica volume percentages regardless of the initial detrital illite-mica. The degree of smectite diagenesis can be determined by the illite-smectite crystallinity based on the proportion of illite in the illite-smectite complex (e.g. Hower *et al.*, 1976; Shaw and Primmer, 1988). The different mixture of smectite and illite also yield different X-ray diffraction peak positions and intensities which can be used for proportion identification (Raynolds and Hower, 1969).

In the following part, the interpretation relies mainly on the clay content of the samples. Sample #2 has low clay content (< 15 vol.%) and will be excluded from the smectite estimation. The initial smectite data shows a great variation among samples from low and deep depths. However, the average initial smectite volumes for both depths show similar values (~30 vol.%) (Fig. 4.1). According to the computational diffraction pattern of illite-smectite mixed phases by Raynolds and Hower, (1969), the peak position of illite-smectite phase in this study represents an illite-smectite complex which contain between 80% and 100% illite. Hence, our samples are estimated to contain 85% to 95% of illite in the illite-smectite phase.

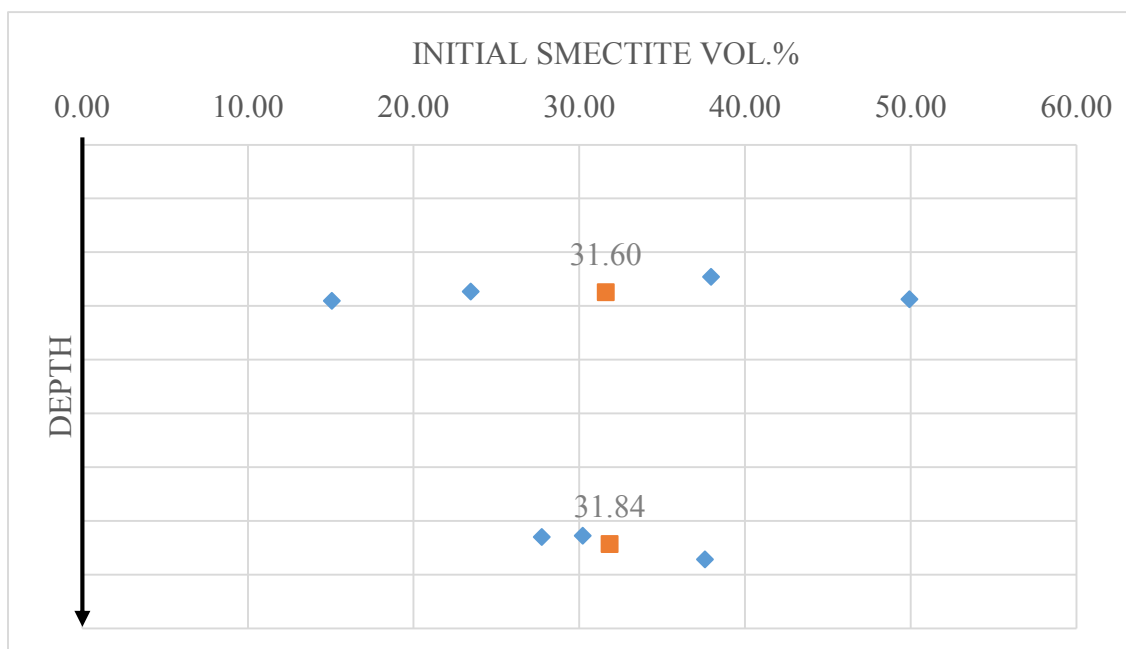


Figure 4.1 Cross plots between initial smectite vol.% in the shales samples from different depth. The blue data points represent the individual data of each samples and the oranges are the average value between the samples from adjacent depth.

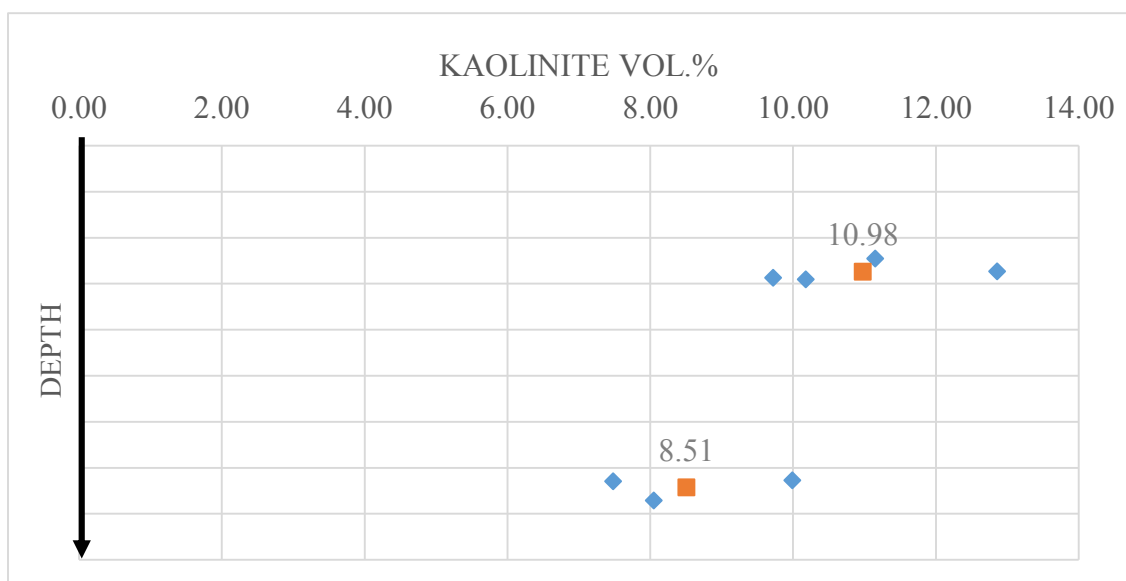
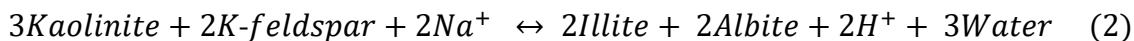


Figure 4.2 The kaolinite vol.% in this study samples. The blue data points represent the individual data of each samples and the oranges are the average value between the samples from adjacent depth.

Another potential clay diagenesis which can increase the pore fluid volume through water expulsion are the transformation of kaolinite to illite reactions which can be summarized by the reactions (Bjørlykke *et al.*, 1998):



or



The kaolinite diagenetic reactions start at higher temperature than the smectite illization which is possibly related to the overpressure zone in the Gulf of Thailand. However, there is no clear observation of kaolinite diagenesis in this study. The difference in kaolinite proportion between samples from two depth apart are minimal (Fig. 4.2). The lack of k-feldspar in shale samples possibly due to the alteration of anorthoclase (orthoclase-albite solid solution) to albite along the (2) reaction path. Nonetheless, the samples contain approximately 10 vol.% of kaolinite, thus the kaolinite diagenesis may not release significant water volume.

A comparison between the initial smectite and degree of diagenesis from this study and previous studies in the Gulf of Mexico (Perry and Hower, 1972; Bruce, 1984) shows that clay diagenesis in the Gulf of Thailand yield less significant fluid volume than that of the Gulf of Mexico (Table 4.1). Shale samples in this study have approximately 30 vol. % while those from the Gulf of Mexico contain about 45 vol.%. As for the degree of diagenesis of illite-smectite, this study shows a difference in illite content of approximately 10% illite (from 85% to 95%) in contrast to the difference of 55% illite (from 25% to 80%). In addition, water expelled through diagenetic process of clay minerals in the study area has less impact on the shale pore pressure than the pore pressure gradient of about 20 kPa/m in the Gulf of Mexico suggesting that other factors simultaneously contribute to the increase in pore pressure. Moreover, the reason behind the significant differences between the illite content is possibly caused by different geothermal gradient. The Gulf of Thailand has higher geothermal gradient (45-70 °C/km) than the Gulf of Mexico (15-25 °C/km) (Bustin and Chonchawalit, 1995; Morley, *et al.*, 2013; Christie and Nagihara, 2015). Thus, smectite from the Gulf of Thailand has been altered prior to the depth of investigation. Results suggest that there is no direct correlation between the diagenesis zone of smectite and overpressure zone unlike those of the Gulf of Mexico (Shaw and Primmer, 1988).

Table 4.1 Comparison between initial smectite volumes, degree of diagenesis and pore pressure gradients of the Gulf of Thailand (this study) and the Gulf of Mexico (Perry and Hower, 1972; Bruce, 1984).

	Gulf of Mexico	This study
Initial smectite	~ 45 vol.%	~ 30 vol.%
Degree of diagenesis	25 → 80 % illite	85 → 95 % illite
Pore pressure gradient	19-21 kPa/m	N/A

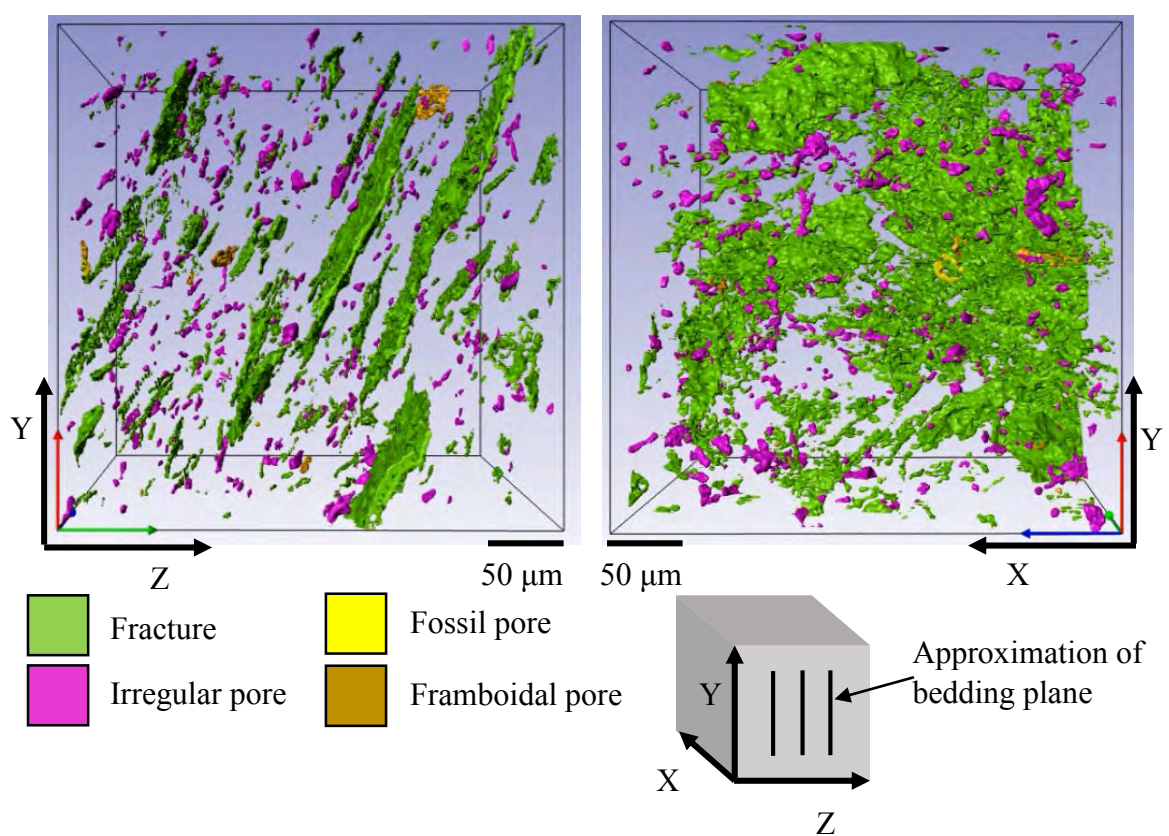


Figure 4.3 An example of shale 3D segmented porosity model. The pore mainly consist of irregular pores and fractures. The fractures align almost parallel to the bedding plane.

4.2 Porosity analysis

The segmentation of 3D porosity shows that shales from the Gulf of Thailand possess low and discrete pore system (Fig. 4.3). The separated pores prohibit the pore fluid transfer therefore, enable the pore pressure build up as the water expelled (Bruce, 1984). While the most abundant pore types of shale samples in this study are fracture and irregular kerogen-filled pores, a study by Loucks, *et al.* (2012) shows that nano-scale pores in shale are consist mainly of interparticle pore, intraparticle pore and organic matter pore. Even though several factors such as organic matter type, content and mineralogy control the variety of pore network, it is possible that the Gulf of Thailand shale may contain more tiny pores which are under the image resolution hence, undetectable via SXRT experiment. Moreover, organic matter pore and interparticle pore tend to connect the effective pore network and allow fluid flow (McCreesh *et al.*, 1991; Loucks *et al.*, 2009). However, low permeability due to nano to micro scale pore throat may retain the pore fluid and increase pore pressure.

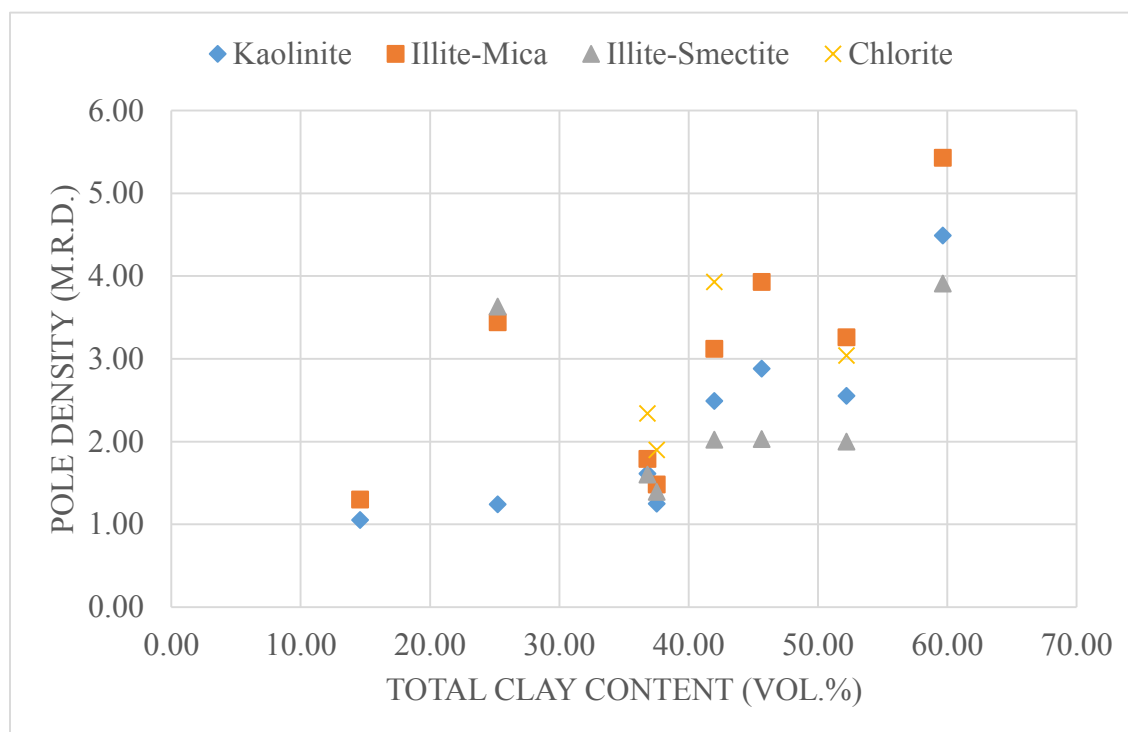


Figure 4.4 Total clay content vs. maximum pole density cross plots, each data point represent the individual pole density of respective mineral (001) lattice plane. These data show an increasing trending of pole density with clay content.

4.3 Preferred orientation

All phyllosilicate minerals in this study show a preferred orientation of a (001) lattice paralleled to the bedding plane. The preferred orientation of clay minerals derived from the Rietveld analysis shows that the maximum pole density of clay orientation increase correspondingly with total sample clay content (Fig. 4.4). However, no clear relation function between clay content and degree of preferred orientation can be stated, except that degree of preferred orientation tends to increase with clay content. Moreover, the comparison between the preferred orientation averages of shallow and deep samples shows no distinguishable trends, suggesting that the different confining pressure has little to no effect on the clay mineral preferred orientation in this study (Fig. 4.5).

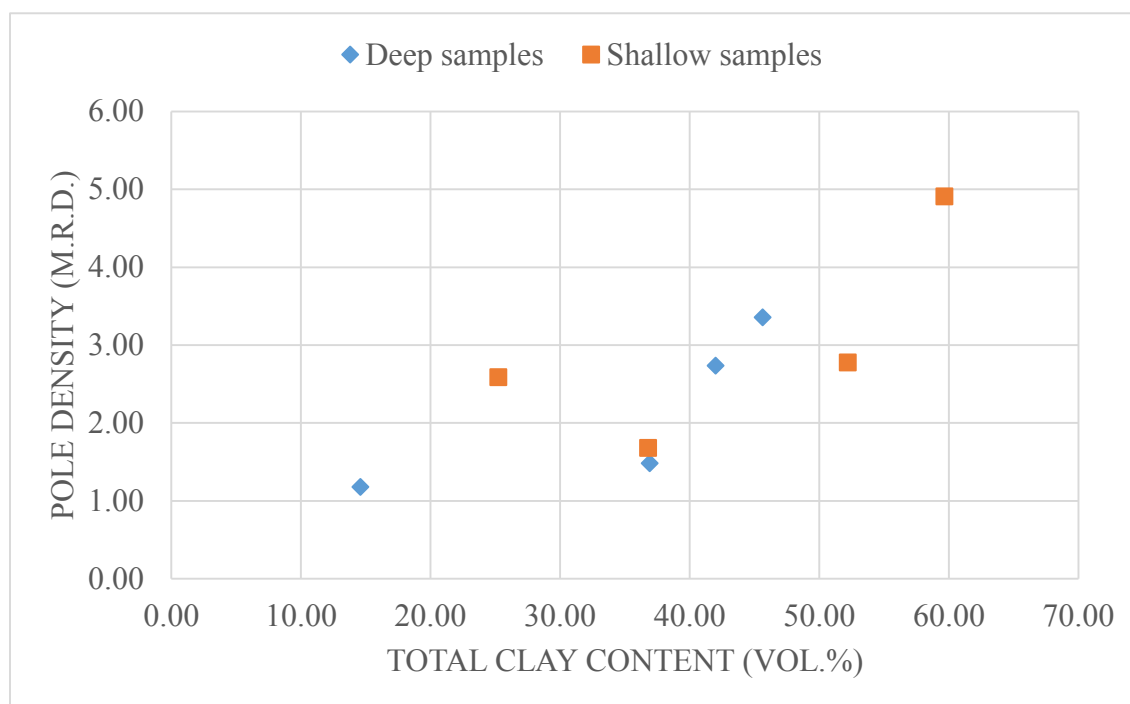


Figure 4.5 Cross plots between weight-averages of maximum pole density and total clay content for each samples. Comparison between shallow (orange) and deep (blue) samples shows similar trend of pole density with increasing clay content.

Chapter V: Conclusions

5.1 Conclusions

The main focuses of this study is about an effect on pore fluid from smectite illization and pore network of shale samples from the Gulf of Thailand. The synchrotron X-ray diffraction analysis shows that the samples contain a significant clay content, especially illite-smectite and illite-mica. However, only small amount of smectite is converted to illite within the overpressure zone. Consequently, clay diagenesis can only yield minor pore fluid and has minor impact to pore pressure build up in this area. The overpressure in this area is thus, mainly accompanied by other factors. The 3D reconstruction images of shales from the synchrotron X-ray microtomography generally show a low porosity volume and contain a wide range of micron-size pore types. The dominant pore type is fracture and kerogen-filled irregular pores. Small, discrete pores make up the majority of pore volumes and are randomly scattered in the matrix. The dispersion of these pores may play an important role in pore pressure build up as they restrict fluid flow.

5.2 Future works

Due to the high heterogeneity of shale, more rock samples are need to minimize the sampling bias. In the basin with high geothermal gradient, sample collection should be extended above the top of overpressure zone in order to clearly understand the changes with depth. This is because the diagenetic reaction possibly start prior to the depth of overpressure. Correlation with formation pore pressure from the actual well data is suggested in order to investigate the causes of overpressure and improve pore pressure prediction technique. The investigation for nano pores should be carried out in order to thoroughly understand the actual pore network of shales and how the pore fluid is stored.

References

- Bjørlykke, K. Clay mineral diagenesis in sedimentary basins - a key to the prediction of rock properties. Examples from the North Sea Basin. Clay Minerals 33, 1998): 15-34.
- Bruce, C. H. Smectite dehydration-Its relation to structural development and hydrocarbon accumulation in Northern Gulf of Mexico Basin. The American Association of Petroleum Geologist Bulletin 68, 6(1984): 637-683.
- Bustin, R. M. and Chonchawalit, A. Formation and Tectonic Evolution of the Pattani Basin, Gulf of Thailand. International Geology Review 37,10(1995): 866-892
- Christie, C. H. and Nagihara, S. Geothermal gradients of the northern continental shelf of the Gulf of Mexico. Geosphere 12, 1(2015): 1-9.
- Eaton, B. A. Graphical method predicts geopressures worldwide. World Oil 76, 7(1972): 100-104.
- Ho, N.-C., Peacore, D. R. and Van der Pluijm, B. A. Preferred orientation of phyllosilicates in Gulf Coast mudstone and relation to the smectite-illite transition. Clays and Clay minerals 47, 4(1999): 495-504.
- Hower, J., Eslinger, E. V., Hower, M. E. and Perry, E. A. Mechanism of burial metamorphism of argillaceous sediment: 1. Mineralogical and chemical evidence. Geological Society of America Bulletin. 87, 1976): 725-737.
- Kanitpanyacharoen, W., Kets, F. B., Wenk, H.-R. and Wirth, R. Mineral Preferred Orientation and Microstructure in the Posidonia Shale in Relation to Different Degree of Thermal Maturity. Clays and Clay minerals 60, 3(2012): 315-329.
- Klahan, I. and Nopsuri, W. Real-Time Pore Pressure Gradients: An Example from the Pattani Basin from AAPG International Convention and Exhibition, Search and Discovery Article #41075, Nov. 19, 2012.
- Loucks, R. G., Reed, R. M., Ruppel, S. C. and Hammers, U. Spectrum of pore types and networks in mudrocks and a descriptive classification for matrix-related mudrock pores. AAPG Bulletin 96, 6(2012): 1071-1098.
- Loucks, R. G., Reed, R. M., Ruppel, S. C. and Jarvie, D. M. Morphology, genesis, and distribution of nanometer-scale pores in siliceous mudstones of the Mississippian Barnett Shale. Journal of Sedimentary Research 79, 2009): 848-861.
- McCreech, C. A., Erlich, R. and Crabtree, S. J. Petrography and reservoir physics II: Relating thin section porosity to capillary pressure, the association between pore types and throat size. AAPG Bulletin 75, 1991): 1563-1578.
- Morley, C. K. and Andrew, R. Tertiary stratigraphy. In Ridd, M. F.; Barber, A. J. and Crow, M. J., eds. The Geology of Thailand, 223-271. London: Geological Society, 2011.

- Osborne, M. J. and Swarbrick, R. E. Mechanisms for generating overpressure in sedimentary basins: a reevaluation. AAPG Bulletin 81, 6(1997): 1023-1041.
- Perry, E. A. and Hower, J. Late-stage dehydration in deeply buried pelitic sediments. AAPG Bulletin 56, 1972): 2013-2021.
- Raynolds, R. C. and Hower, J. The Nature of Interlayering in Mixed-layer Illite-Montmorillonites. Clays and Clay minerals 18, 1970): 25-36.
- Shaw, H. F. and Primmer, T. J. Diagenesis in shales from a partly overpressured sequence in the Gulf Coast, Texas, USA. Marine and Petroleum Geology 6(1989): 121-128.
- Suwannasri, K., Promrak, W., Utitsan, S., Chaisomboonpan, V., Groot, R. J., Sognnes, H. I. and Morley, C. K. Reducing the variation of Eaton's exponent for overpressure prediction in a basin affected by multiple overpressure mechanisms. Interpretation 2, 1(2014): SB57-SB68.
- Tingay, M. R., Hillis, T. R., Swarbrick, R. E., Morley, C. K. and Damit, A. R. Origin of overpressure and pore-pressure prediction in the Baram province, Brunei. AAPG Bulletin 93, 1(2009): 51-74.
- Tingay, M. R., Morley, C. K., Laird, A., Limpornpipat, O., Krisadasima, K., Pabchanda, S. and Macintyre, H. R. Evidence for overpressure generation by Kerogen-to-gas maturation in the northern Malay Basin. AAPG Bulletin 97, 4(2013): 637-672.

Appendices

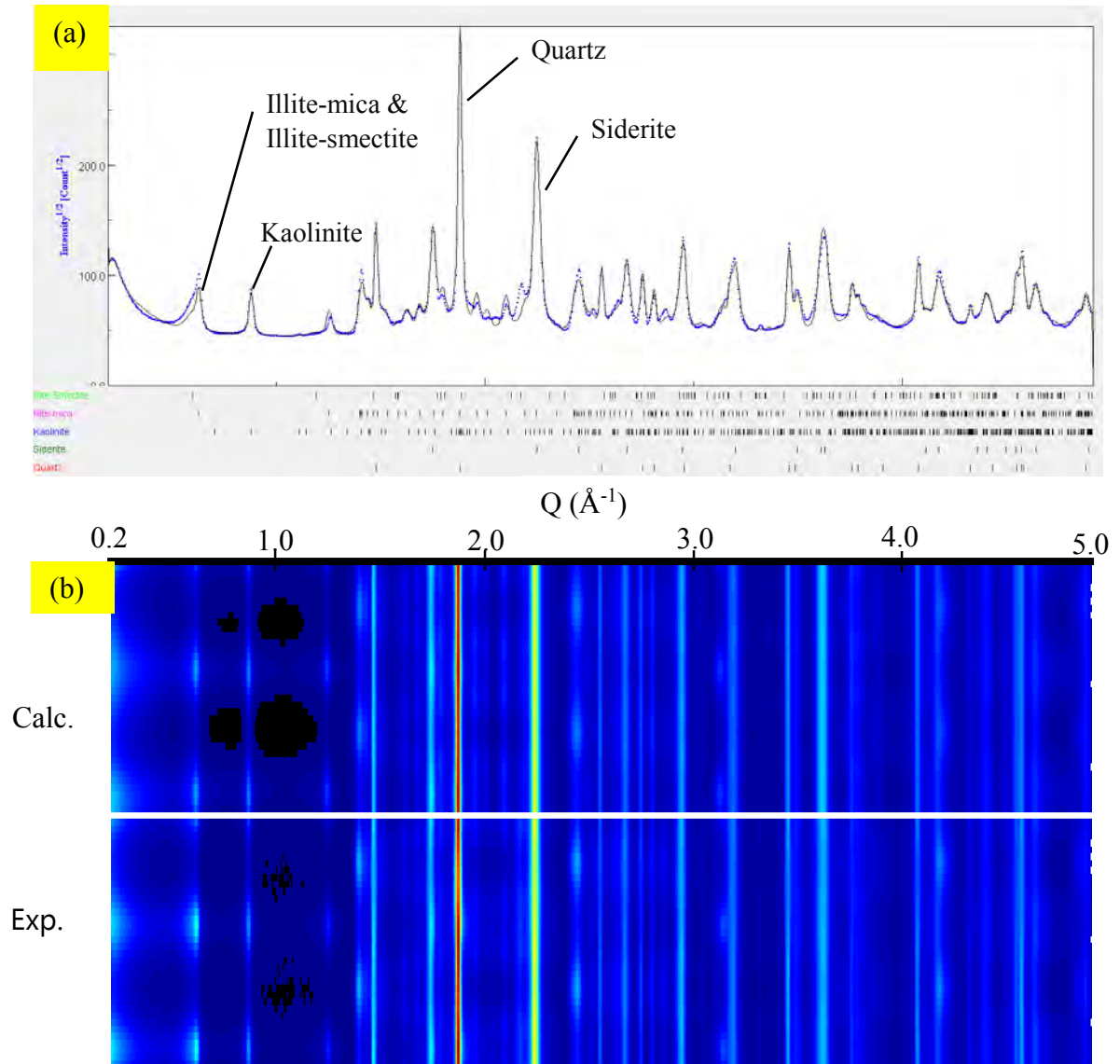


Figure 6.1 (a) A Diffraction peak profile and (b) 2D spectra plot of sample #1

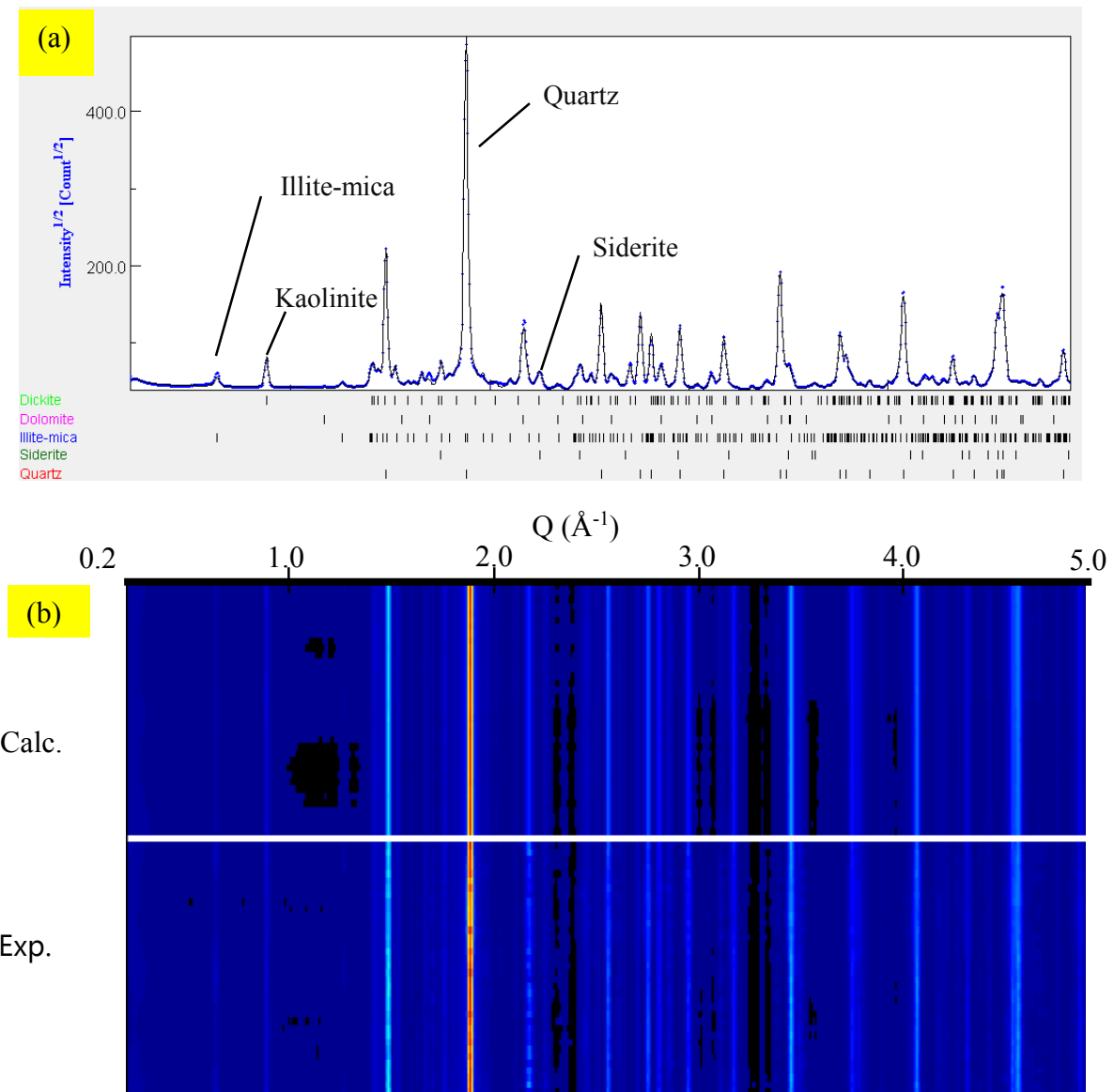


Figure 6.2 (a) A Diffraction peak profile and (b) 2D spectra plot of sample #2

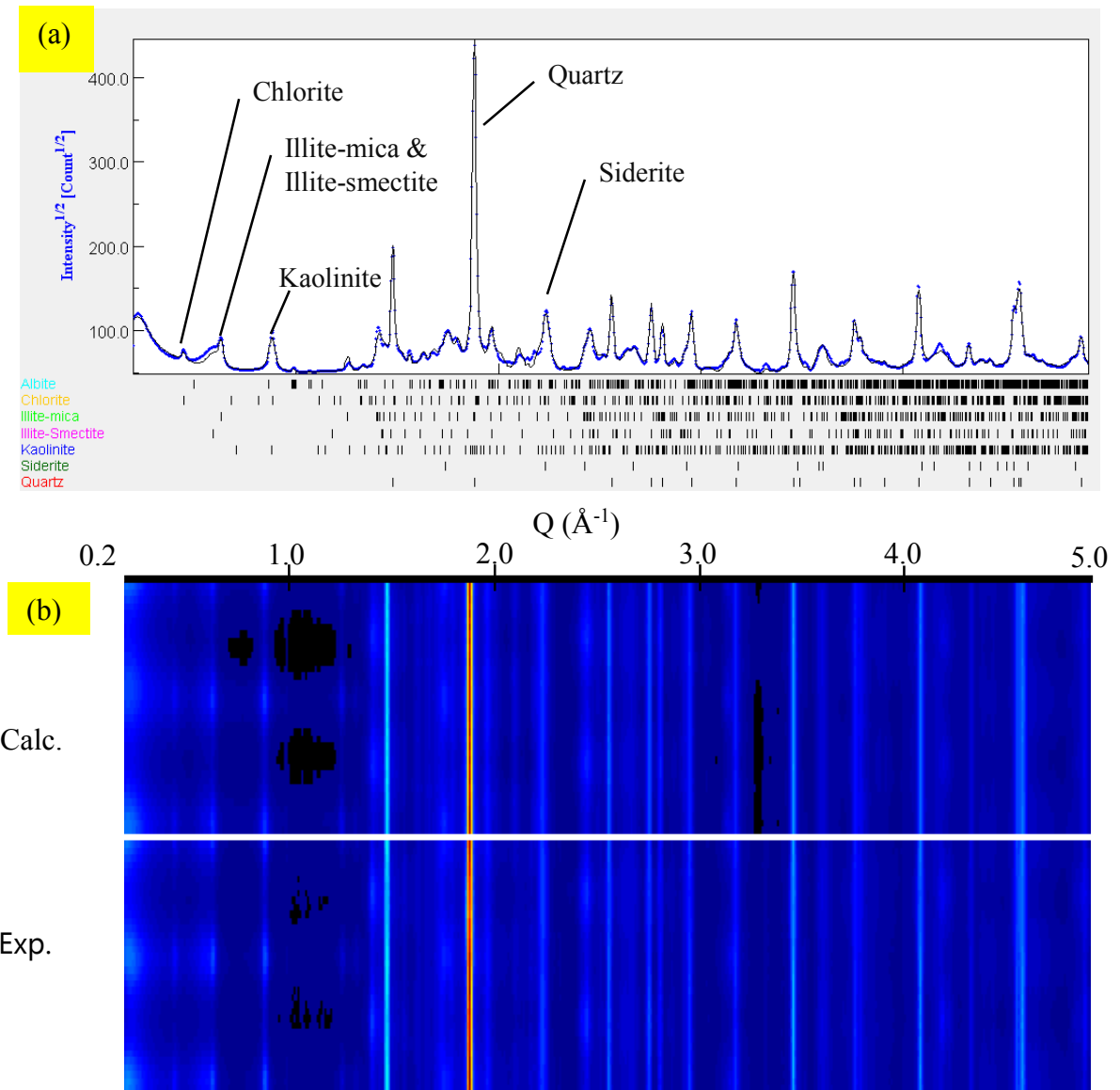


Figure 6.3 (a) A Diffraction peak profile and (b) 2D spectra plot of sample #3

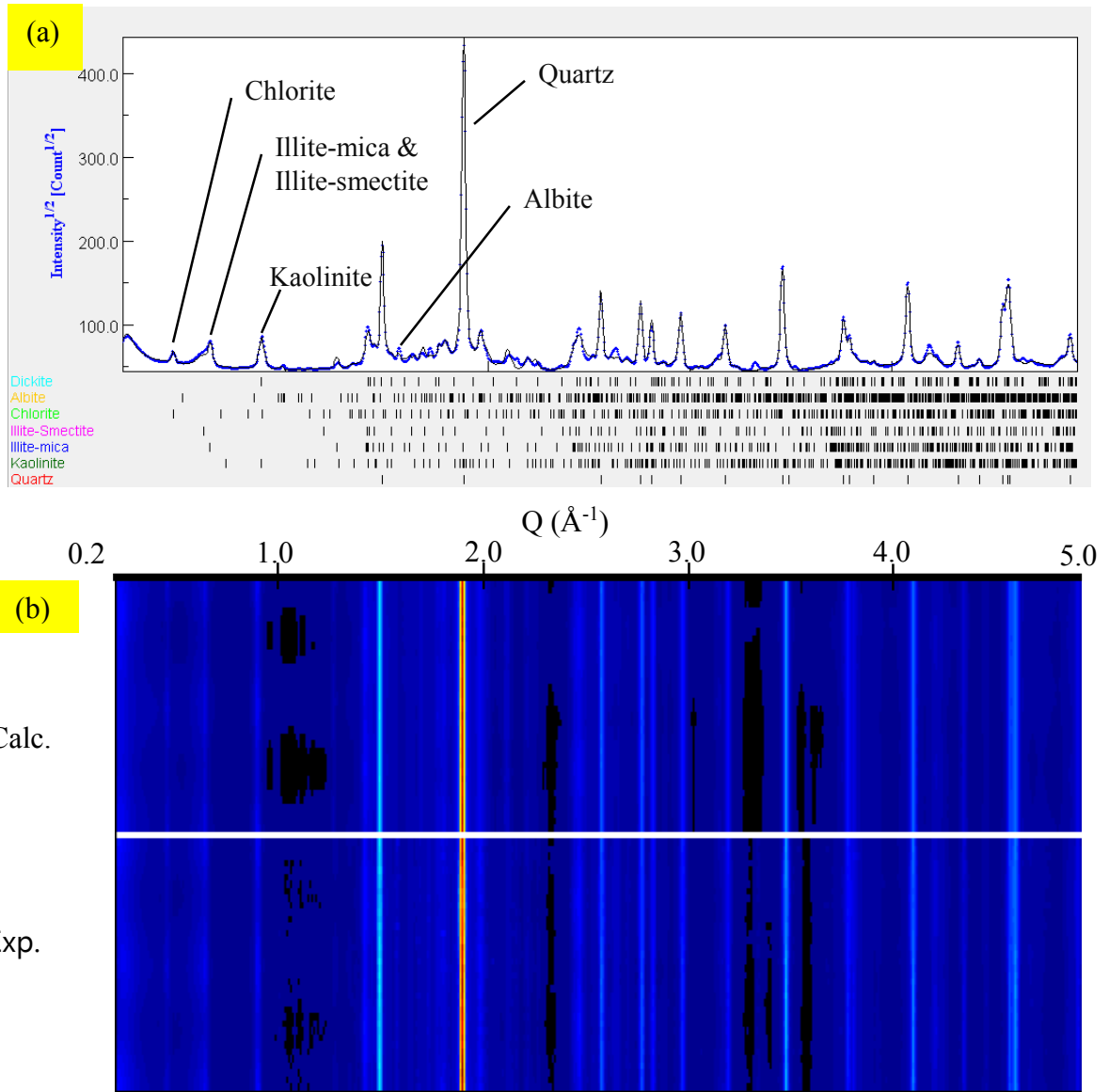


Figure 6.4 (a) A Diffraction peak profile and (b) 2D spectra plot of sample #4

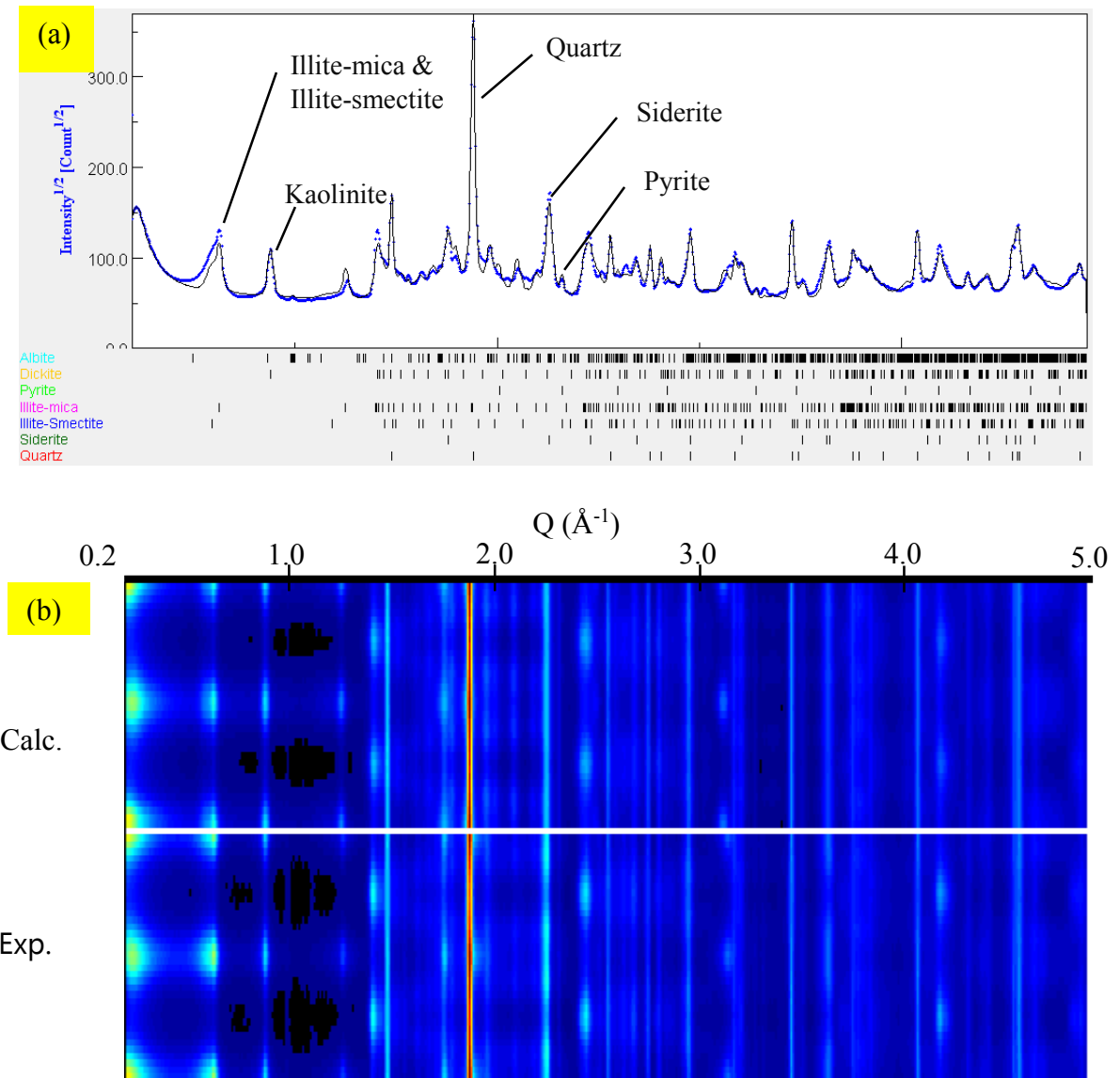


Figure 6.5 (a) A Diffraction peak profile and (b) 2D spectra plot of sample #5

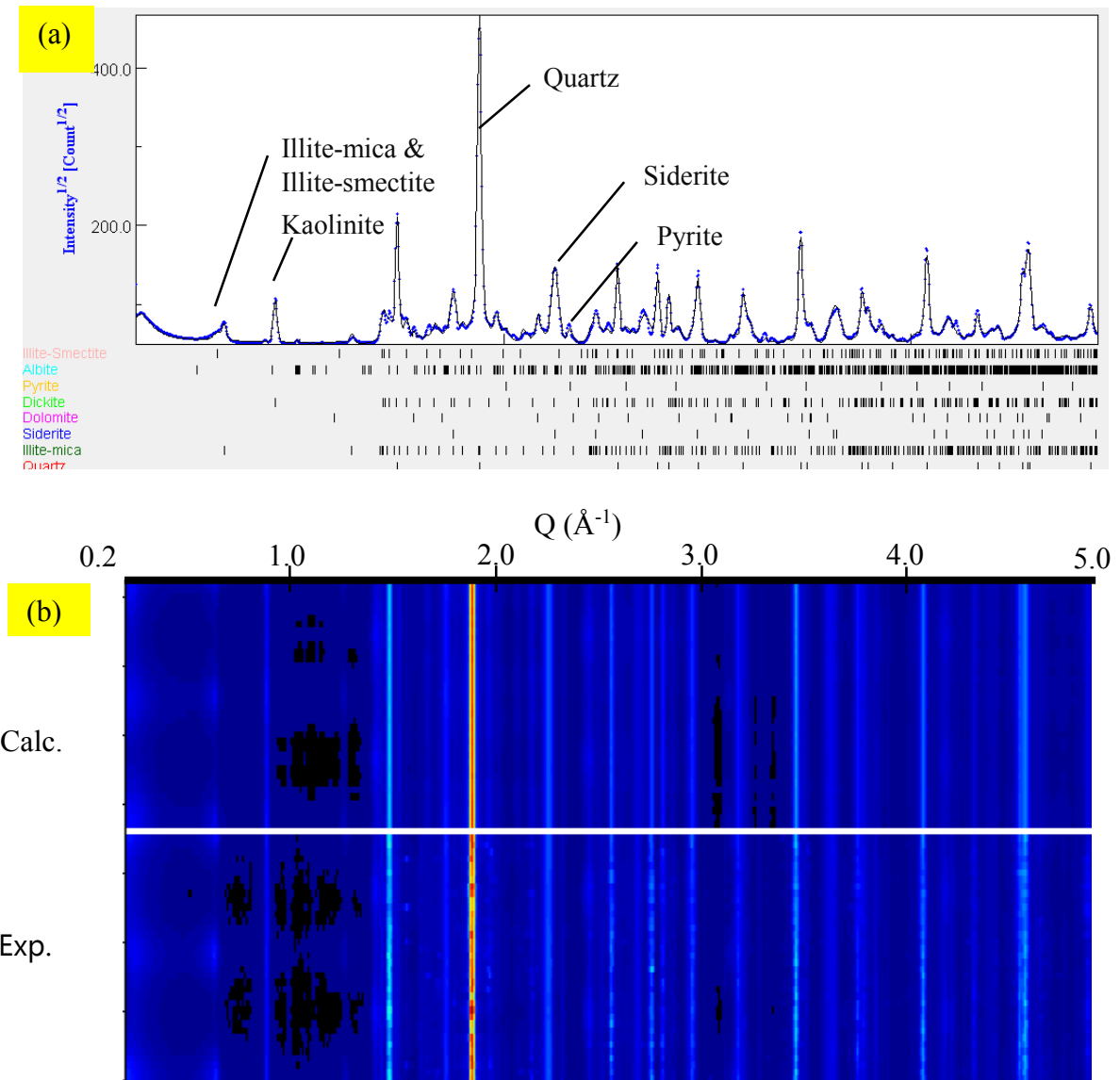


Figure 6.6 (a) A Diffraction peak profile and (b) 2D spectra plot of sample #6

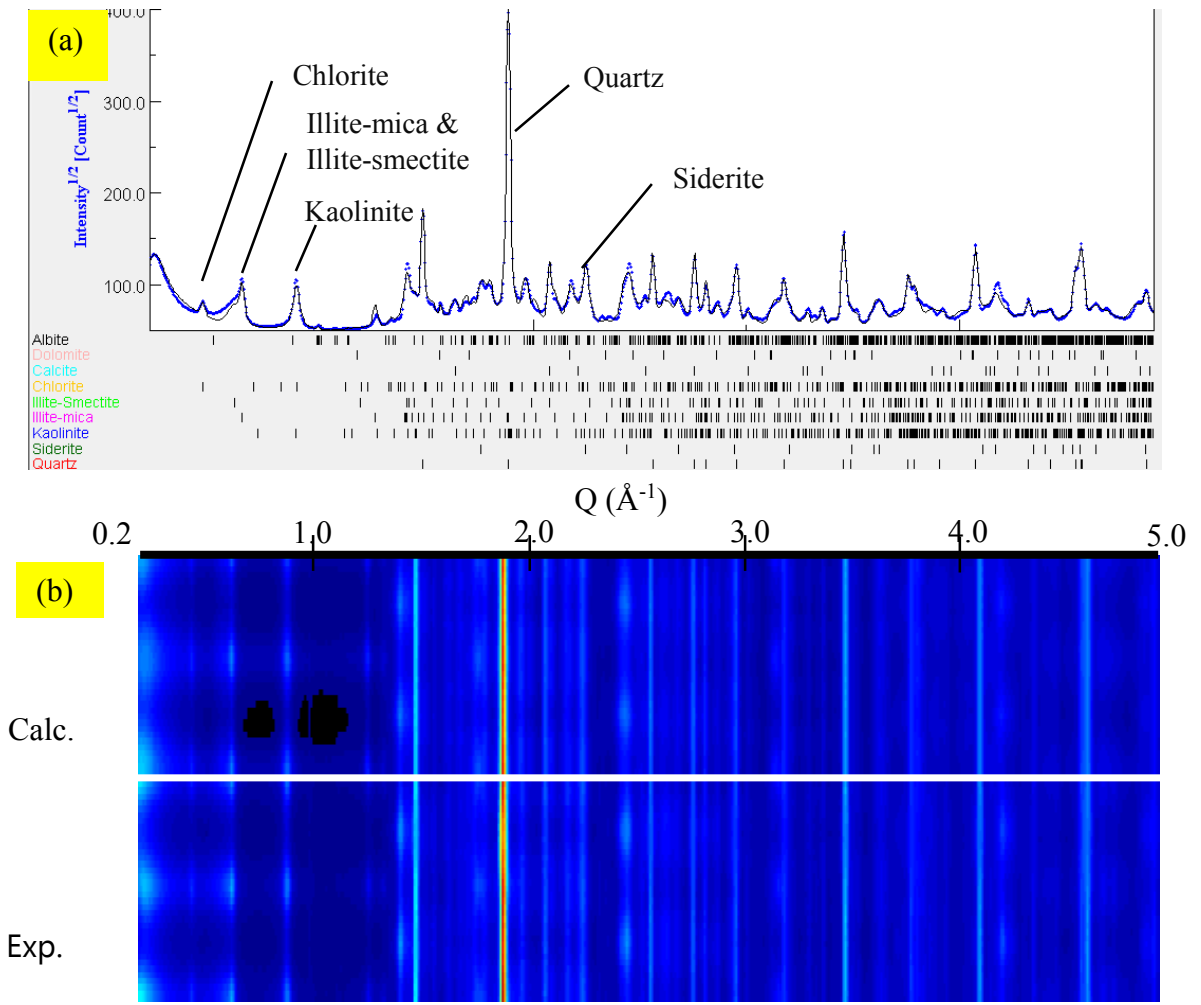


Figure 6.7 (a) A Diffraction peak profile and (b) 2D spectra plot of sample #7

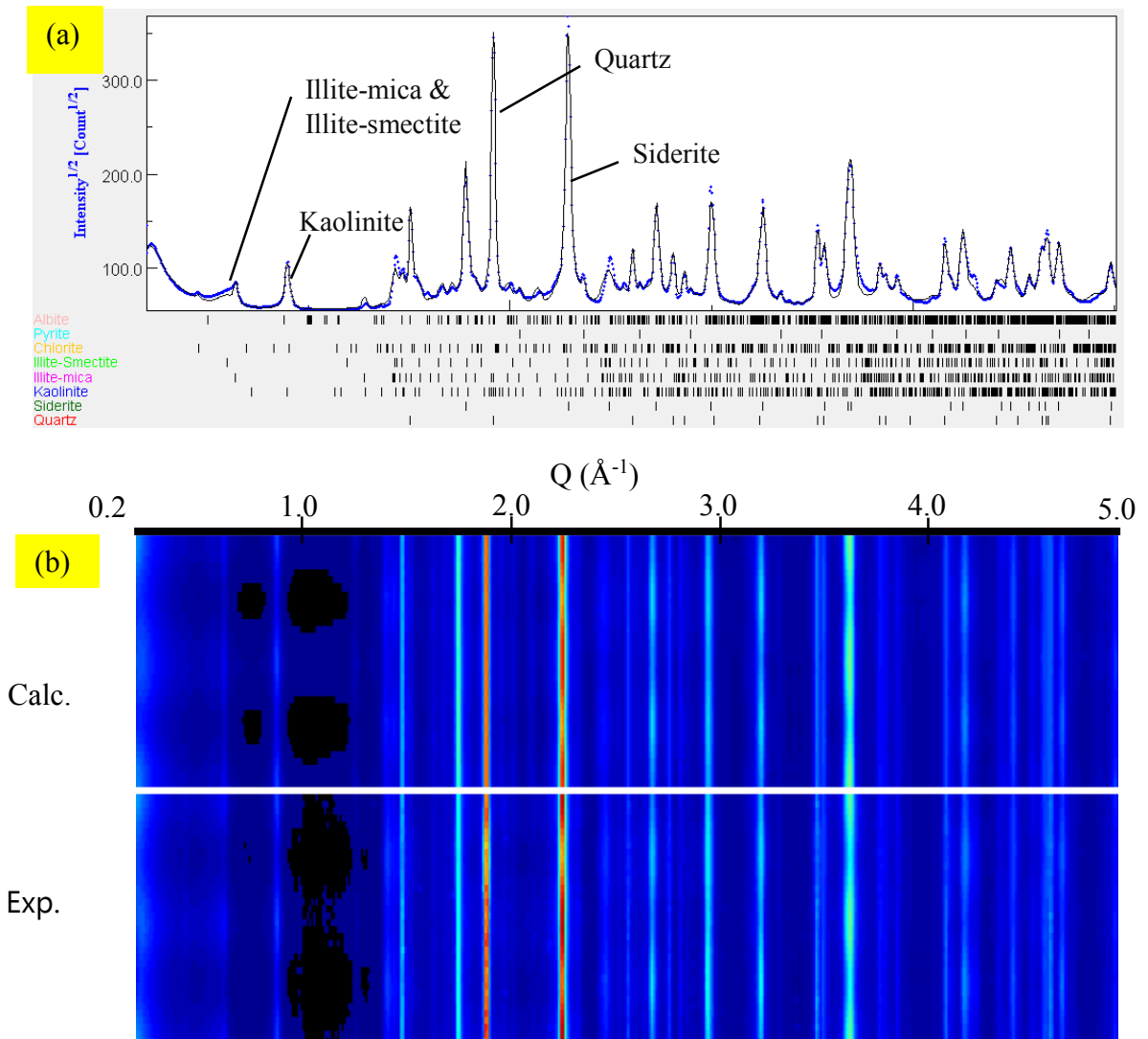


Figure 6.8 (a) A Diffraction peak profile and (b) 2D spectra plot of sample #8